

Structural Determination of Arginine-Linked Cisplatin Complexes via IRMPD Action Spectroscopy: Arginine Binds to Platinum via NO⁻-Binding Mode

C. C. He,^a L. A. Hamlow,^a B. Kimutai,^a H. A. Roy,^a Zachary J. Devereaux,^a N. A. Cunningham,^a
J. K. Martens,^b G. Berden,^b J. Oomens,^{bc} C. S. Chow, and M. T. Rodgers^{a,*}

^aDepartment of Chemistry, Wayne State University, Detroit, Michigan 48202, United States

^bRadboud University, Institute for Molecules and Materials, FELIX Laboratory, Toernooiveld 7c, 6525ED Nijmegen, The Netherlands

^cvan 't Hoff Institute for Molecular Sciences, University of Amsterdam, The Netherlands

Figure Captions

Figure S1. IRMPD spectra of the [(Arg-H)PtCl₂]⁻ and [(Arg)PtCl₂+Na]⁺ complexes in the fingerprint region measured under variable attenuation of the FEL.

Figure S2. Binding modes of Arg to the Pt center of the [(Arg-H)PtCl₂]⁻ complex and the designated nomenclature.

Figure S3. Binding modes of Arg to the Pt center with possible sodium binding modes of the [(Arg)PtCl₂+Na]⁺ complex and the designated nomenclature.

Figure S4. Stable low-energy conformers of the [(Arg-H)PtCl₂]⁻ complex and their relative Gibbs energies at 298 K calculated at B3LYP/mDZP/def2-TZVP level of theory. Structures are classified by the Arg binding mode to Pt.

Figure S5. Stable low-energy conformers of the [(Arg)PtCl₂+Na]⁺ complex and their relative Gibbs energies at 298 K calculated at B3LYP/mDZP/def2-TZVP level of theory. Structures are classified by the Arg binding mode to Pt.

Figure S6. Comparison of the experimental IRMPD spectrum of [(Arg-H)PtCl₂]⁻ with theoretical IR spectra predicted for select NN_s binding conformers along with their optimized structures and relative Gibbs energies computed at B3LYP/mDZP/def2-TZVP level of theory at 298 K. Misaligned IR features are highlighted in red.

Figure S7. Comparison of the experimental IRMPD spectrum of [(Arg-H)PtCl₂]⁻ with theoretical IR spectra predicted for select NO⁻ binding conformers along with their optimized structures and relative Gibbs energies computed at B3LYP/mDZP/def2-TZVP level of theory at 298 K. Misaligned IR features are highlighted in red.

Figure S8. Comparison of the experimental IRMPD spectrum of $[(\text{Arg-H})\text{PtCl}_2]^-$ with theoretical IR spectra predicted for select N_sO^- binding conformers along with their optimized structures and relative Gibbs energies computed at B3LYP/mDZP/def2-TZVP level of theory at 298 K. Misaligned IR features are highlighted in red.

Figure S9. Comparison of the experimental IRMPD spectrum of $[(\text{Arg-H})\text{PtCl}_2]^-$ with theoretical IR spectra predicted for select OO^- binding conformers along with their optimized structures and relative Gibbs energies computed at B3LYP/mDZP/def2-TZVP level of theory at 298 K. Misaligned IR features are highlighted in red.

Figure S10. Comparison of the experimental IRMPD spectrum of $[(\text{Arg-H})\text{PtCl}_2]^-$ with theoretical IR spectra predicted for select conformers with other side chain binding modes along with their optimized structures and relative Gibbs energies computed at B3LYP/mDZP/def2-TZVP level of theory at 298 K. Misaligned IR features are highlighted in red.

Figure S11. Comparison of the experimental IRMPD spectrum of $[(\text{Arg})\text{PtCl}_2+\text{Na}]^+$ with theoretical IR spectra predicted for select NN_s binding conformers along with their optimized structures and relative Gibbs energies computed at B3LYP/mDZP/def2-TZVP level of theory at 298 K. Misaligned IR features are highlighted in red.

Figure S12. Comparison of the experimental IRMPD spectrum of $[(\text{Arg})\text{PtCl}_2+\text{Na}]^+$ with theoretical IR spectra predicted for the NO^- binding conformers along with their optimized structures and relative Gibbs energies computed at B3LYP/mDZP/def2-TZVP level of theory at 298 K. Misaligned IR features are highlighted in red.

Figure S13. Comparison of the experimental IRMPD spectrum of $[(\text{Arg})\text{PtCl}_2+\text{Na}]^+$ with theoretical IR spectra predicted for select N_sO binding conformers along with their optimized structures and relative Gibbs energies computed at B3LYP/mDZP/def2-TZVP level of theory at 298 K. Misaligned IR features are highlighted in red.

Figure S14. Comparison of the experimental IRMPD spectrum of $[(\text{Arg})\text{PtCl}_2+\text{Na}]^+$ with theoretical IR spectra predicted for select OO^- binding conformers along with their optimized structures and relative Gibbs energies computed at B3LYP/mDZP/def2-TZVP level of theory at 298 K. Misaligned IR features are highlighted in red.

Figure S15. Comparison of the experimental IRMPD spectrum of $[(\text{Arg})\text{PtCl}_2+\text{Na}]^+$ with theoretical IR spectra predicted for select conformers with other side chain binding modes along with their optimized structures and relative Gibbs energies computed at B3LYP/mDZP/def2-TZVP level of theory at 298 K. Misaligned IR features are highlighted in red.

Figure S1.

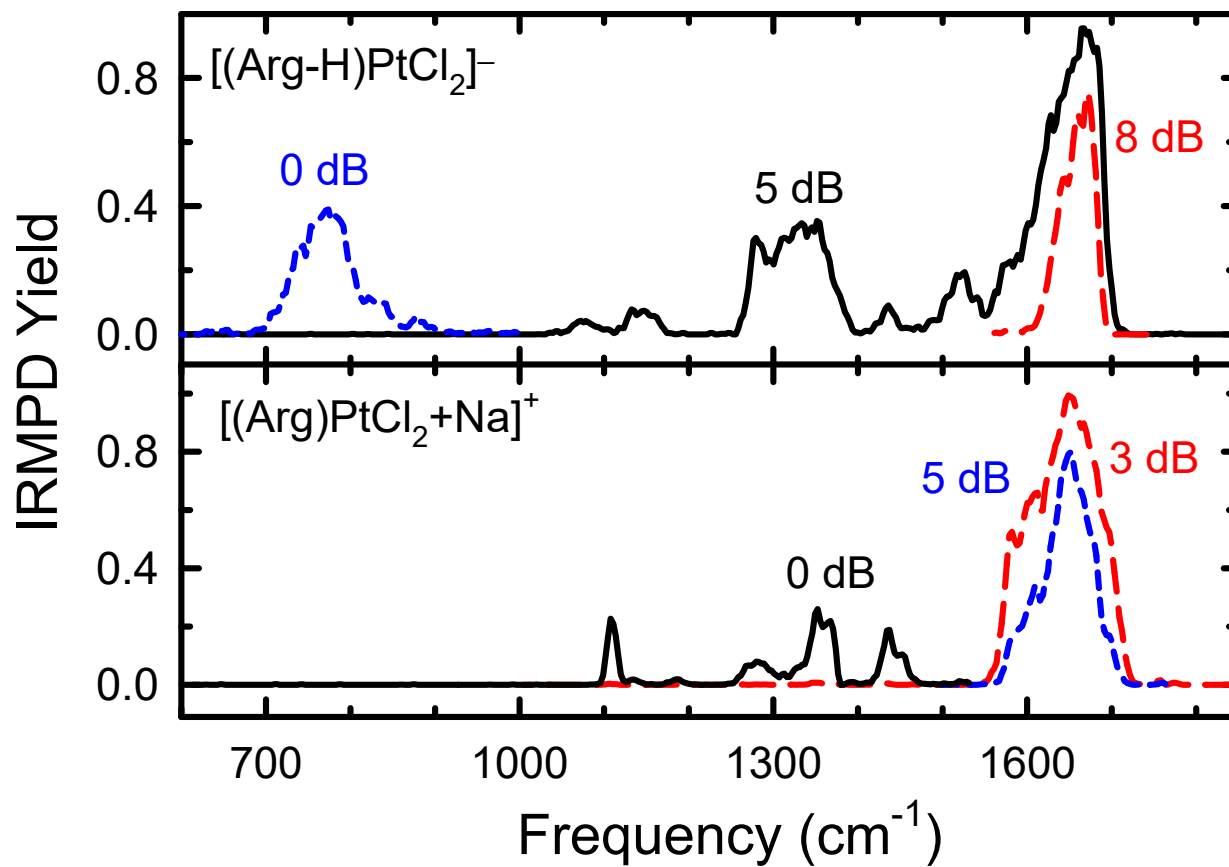


Figure S2.

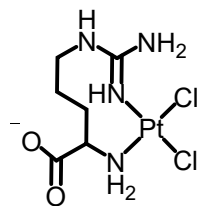
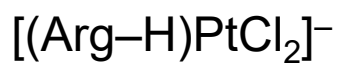
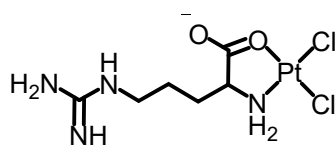
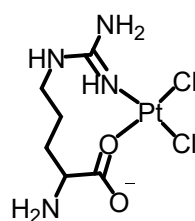
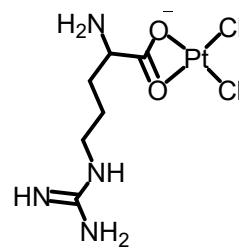
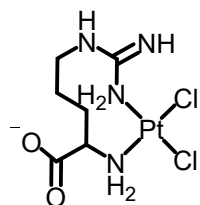
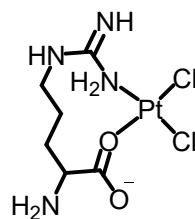
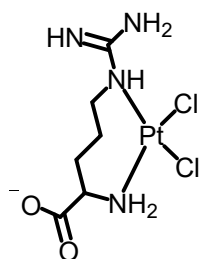
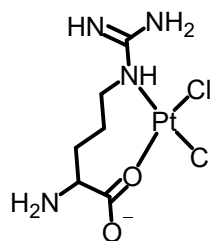
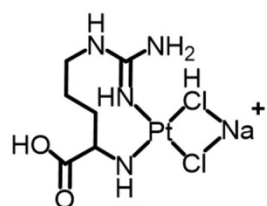
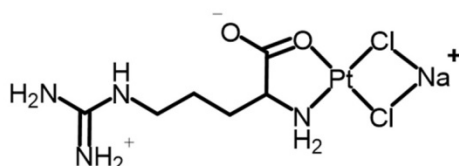
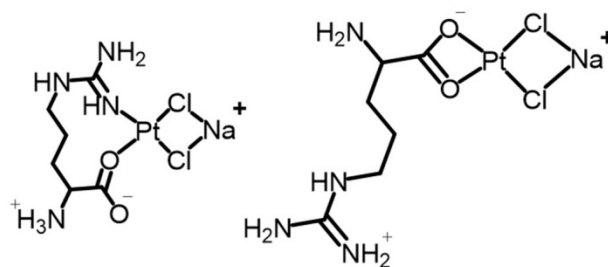
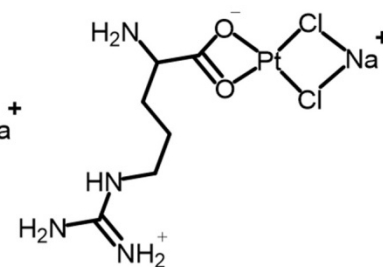
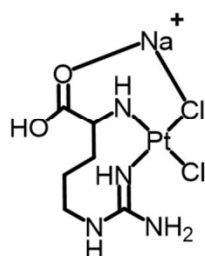
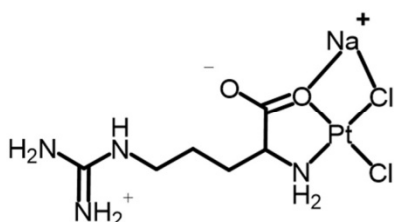
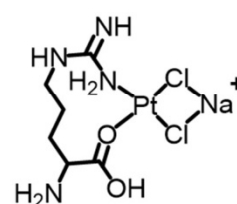
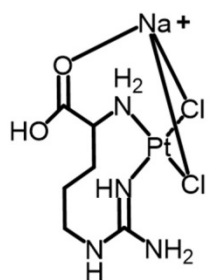
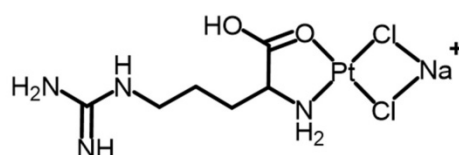
NN_sNO⁻N₅O⁻OO⁻NN_ωN_ωO⁻NN_εN_εO⁻

Figure S3.

NN_sNO⁻N_sO⁻OO⁻NN_s_OCl_sNO⁻_OCl_bN_sONN_s_OCl_bCl_s

NO

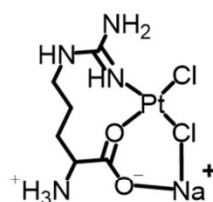
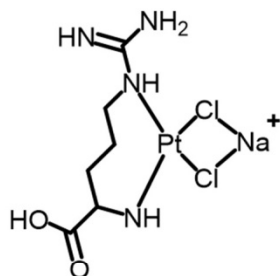
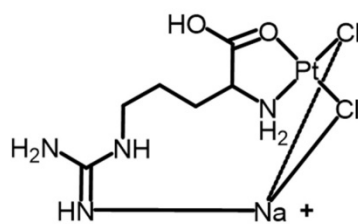
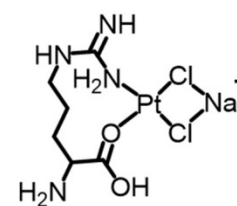
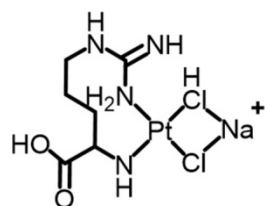
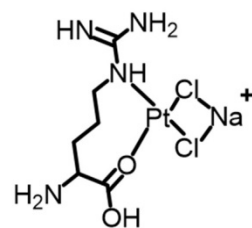
N_sO⁻_OCl_sNN_εNO_{N_s}Cl_bCl_oN_oONN_ωN_εO

Figure S4.

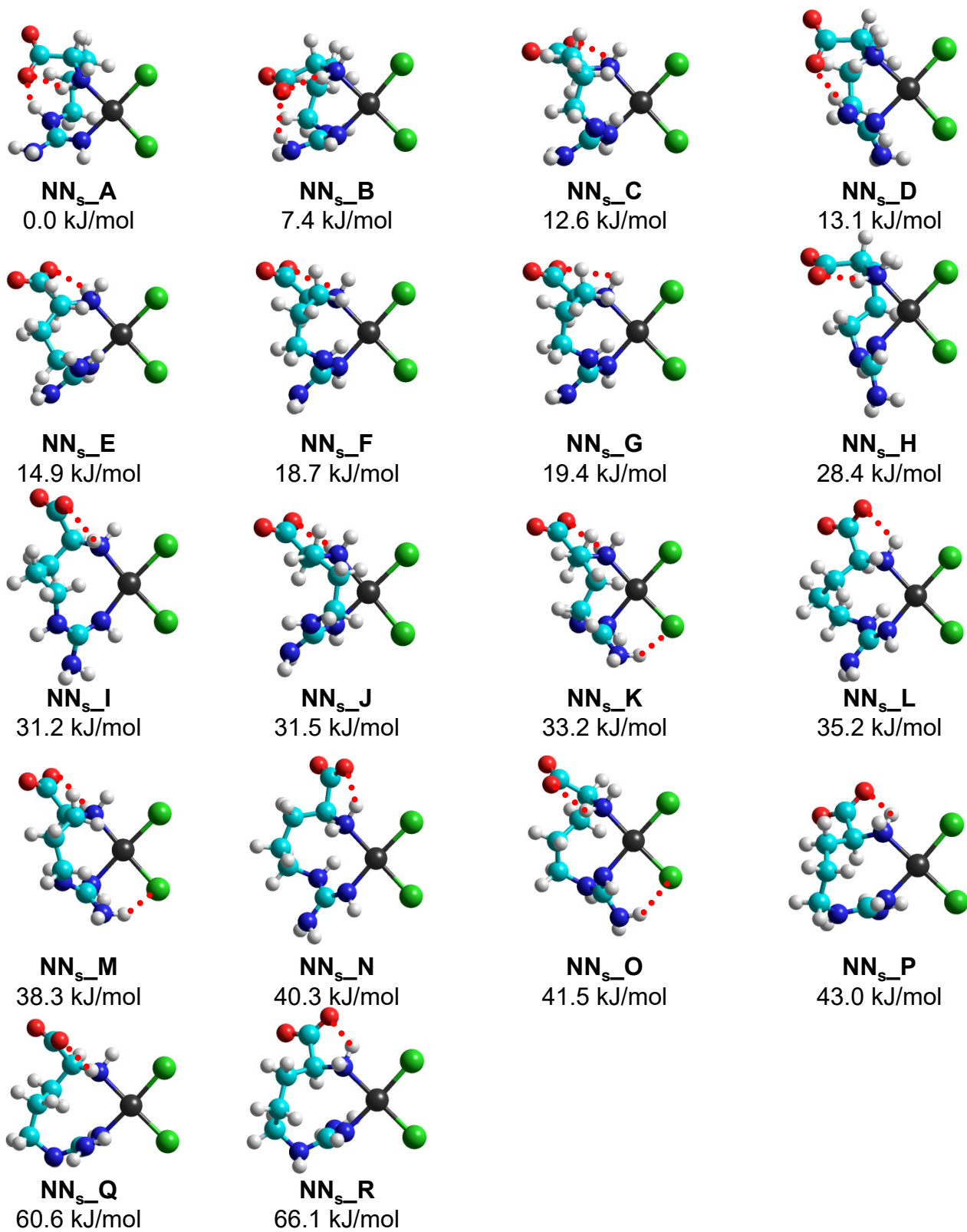


Figure S4.

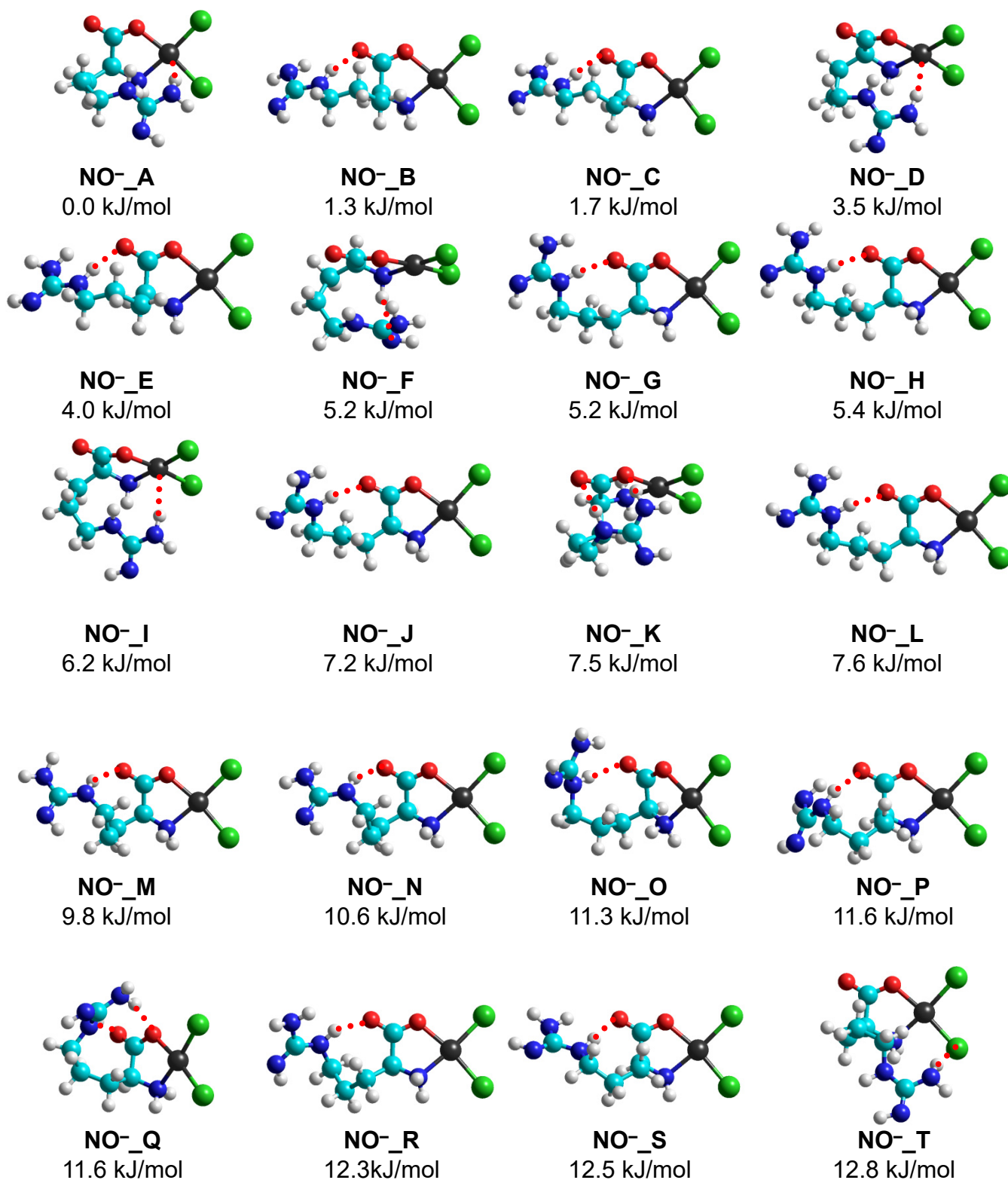


Figure S4.

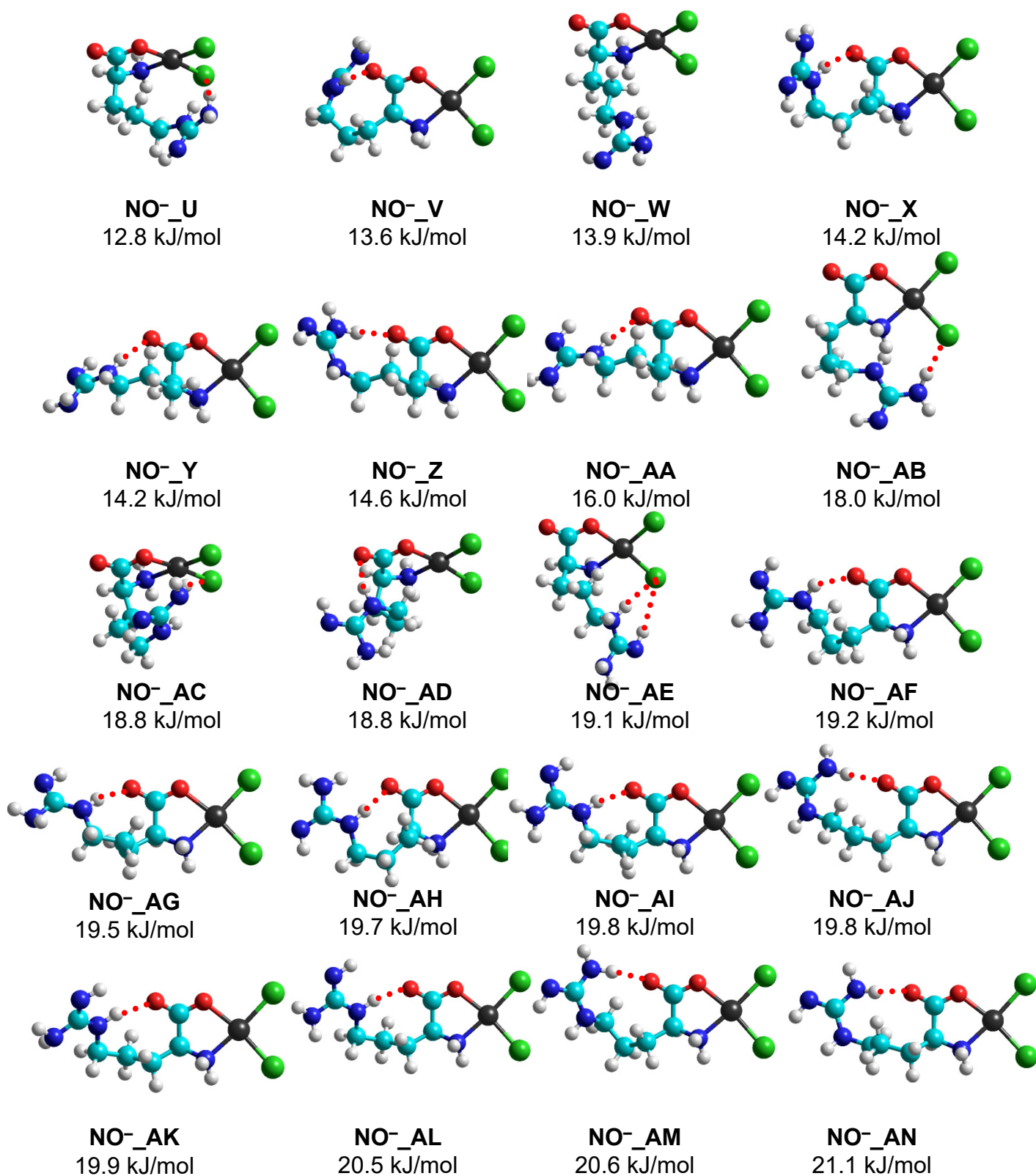


Figure S4.

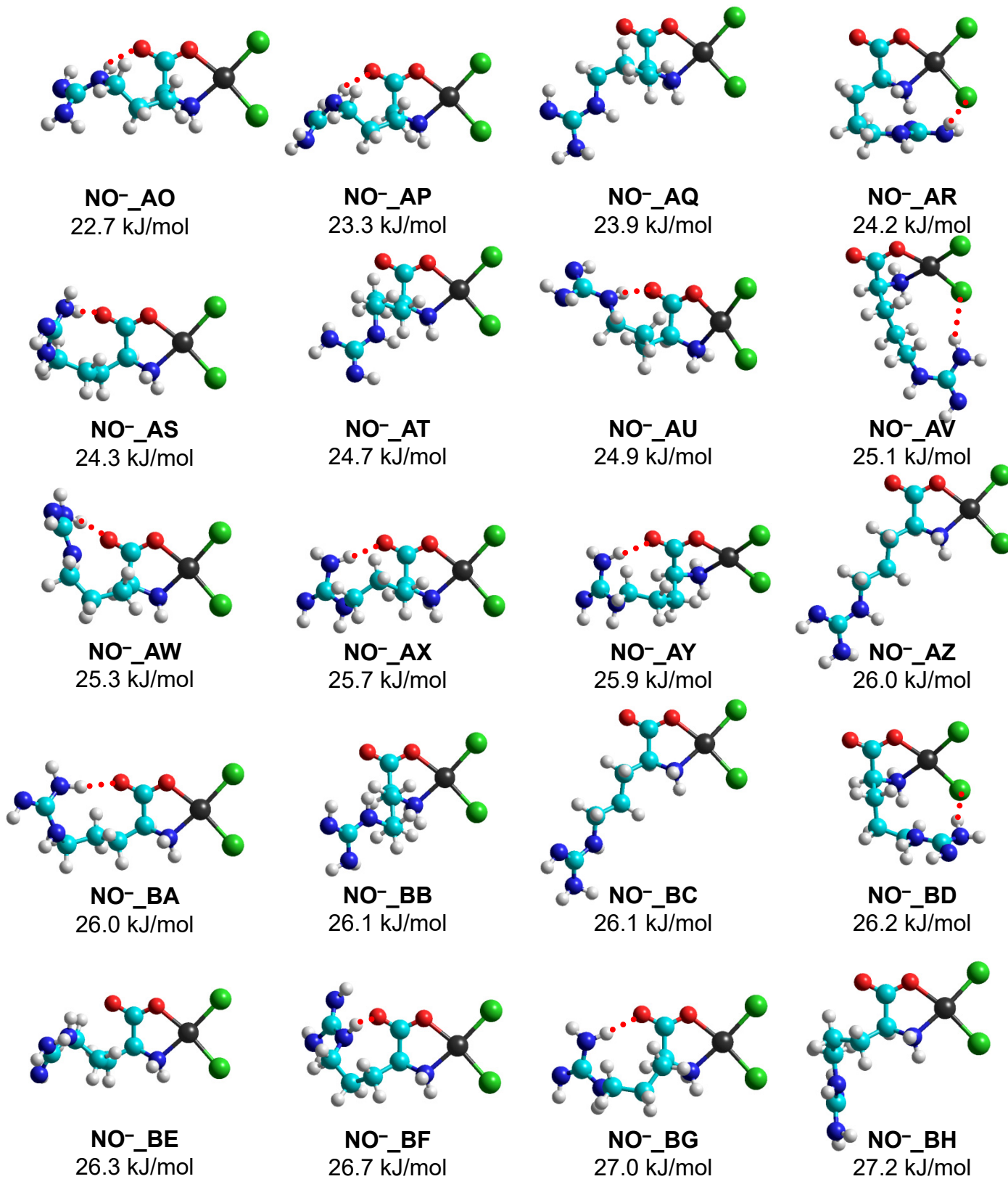


Figure S4.

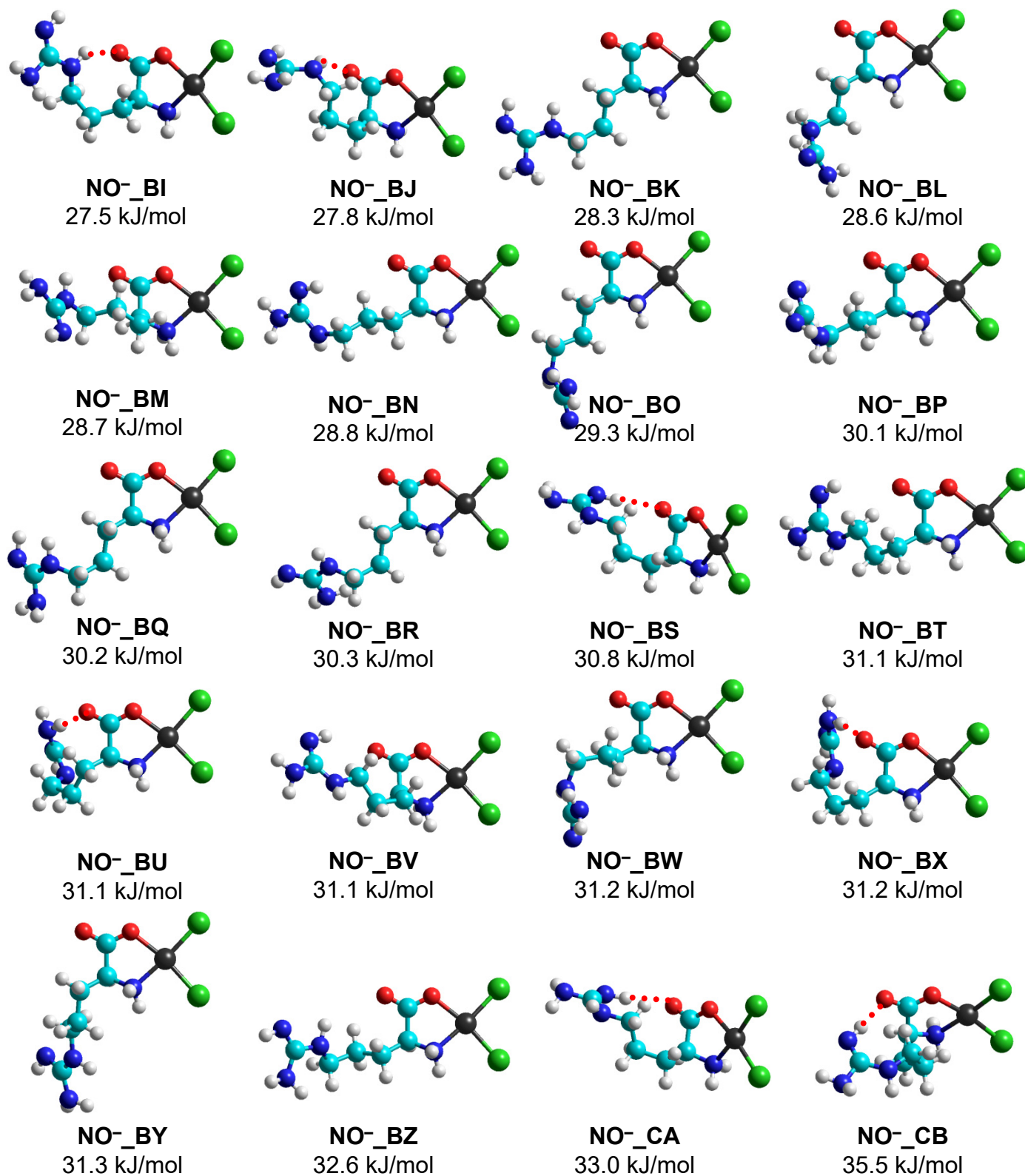


Figure S4.

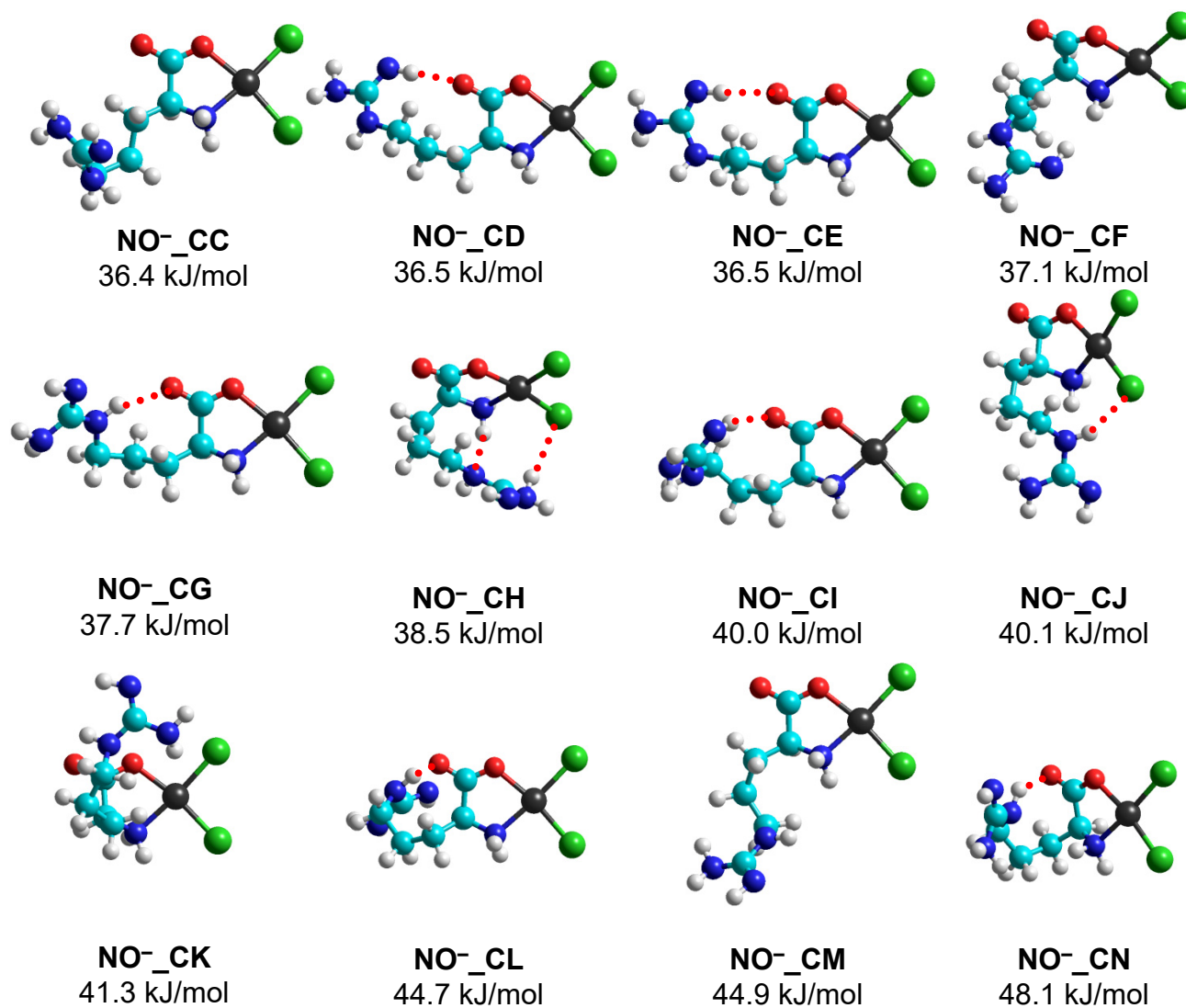


Figure S4.

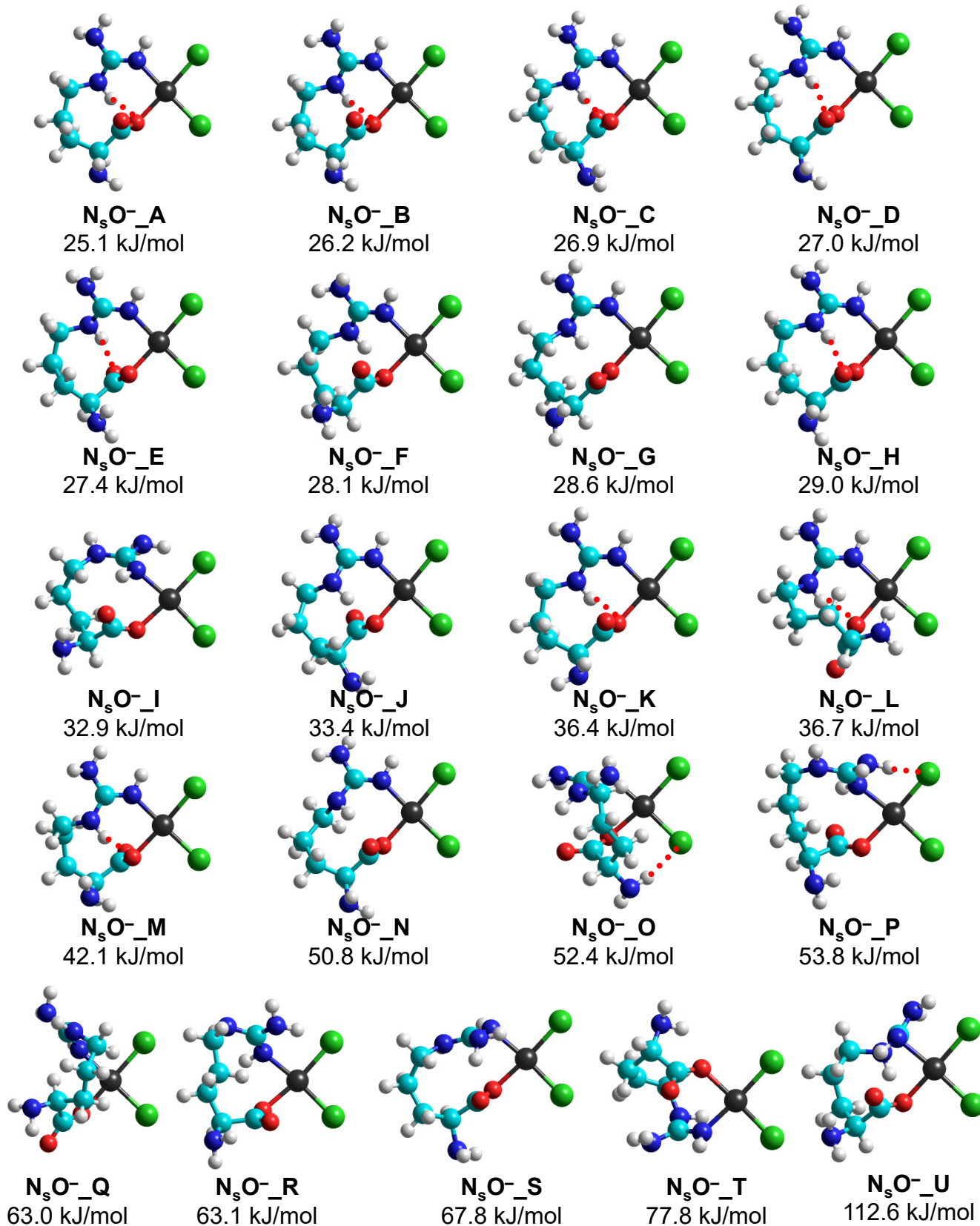


Figure S4.

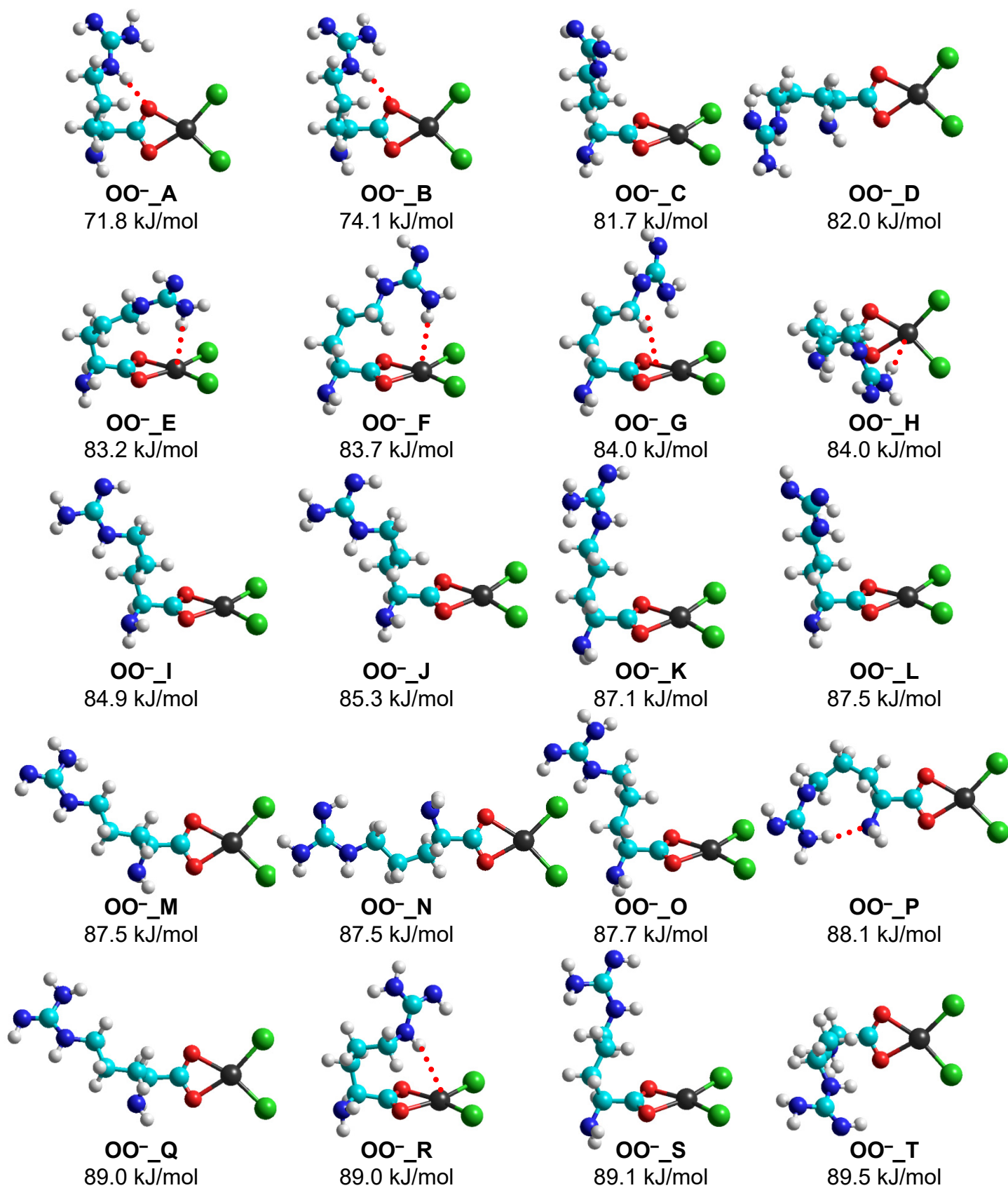
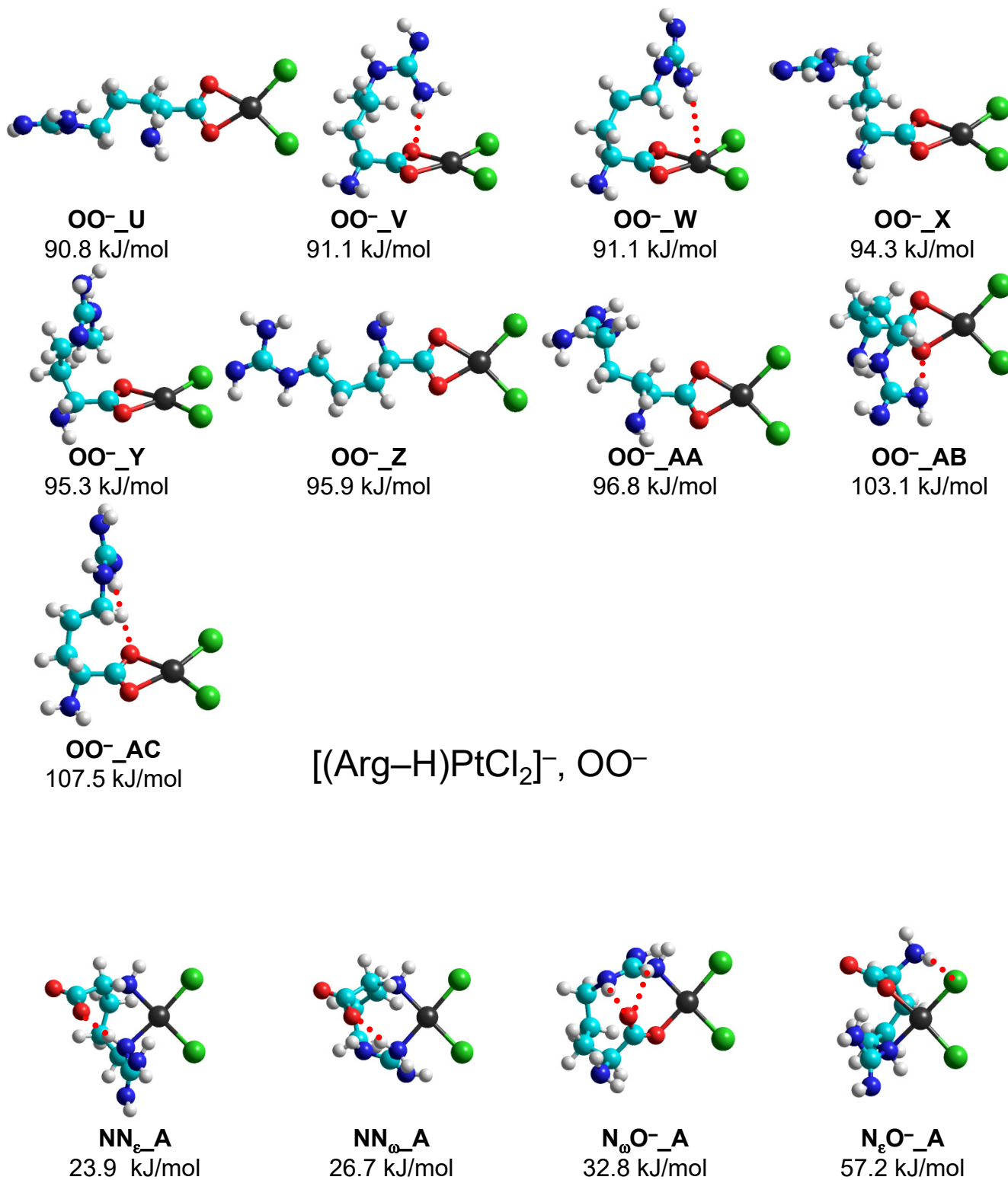
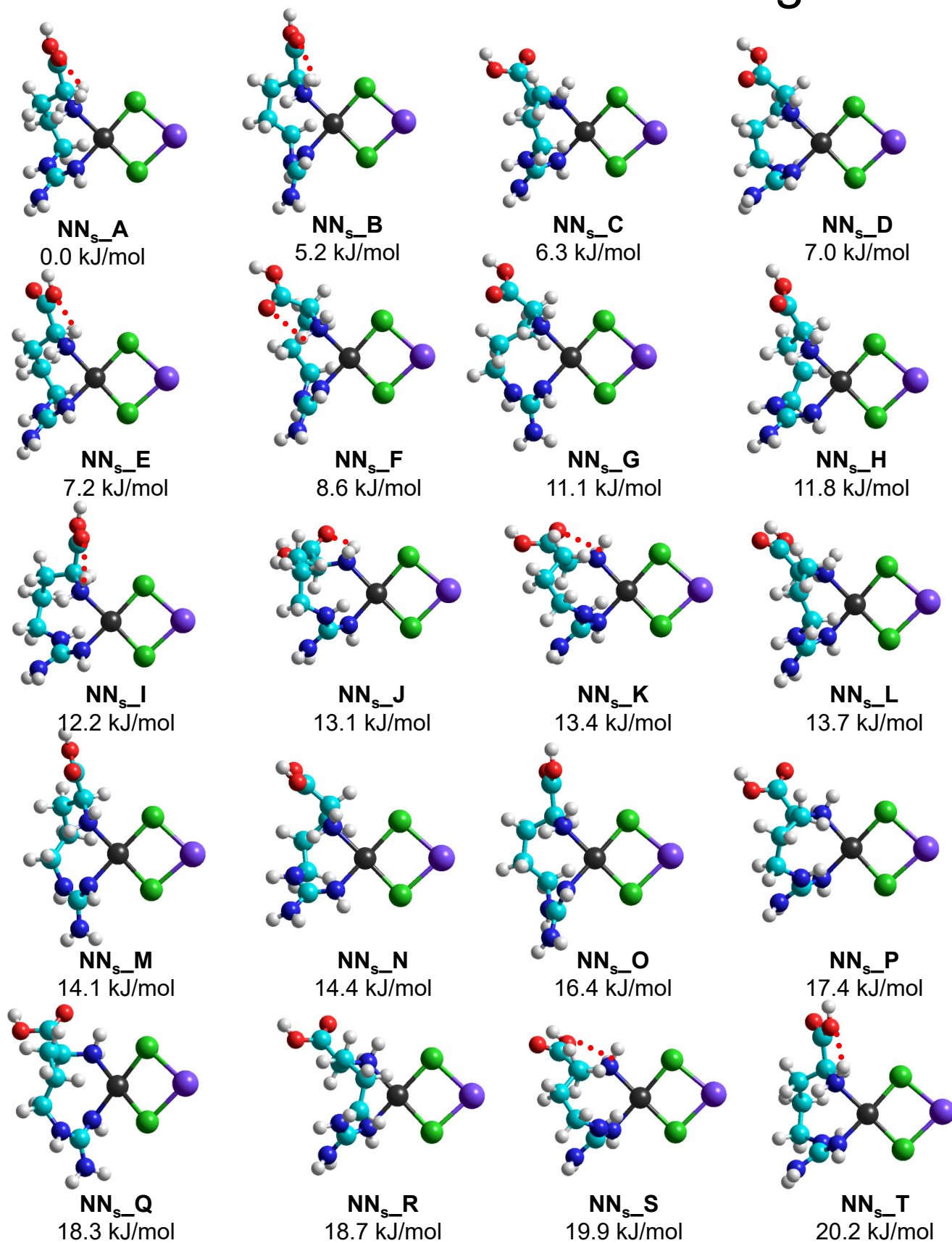


Figure S4.



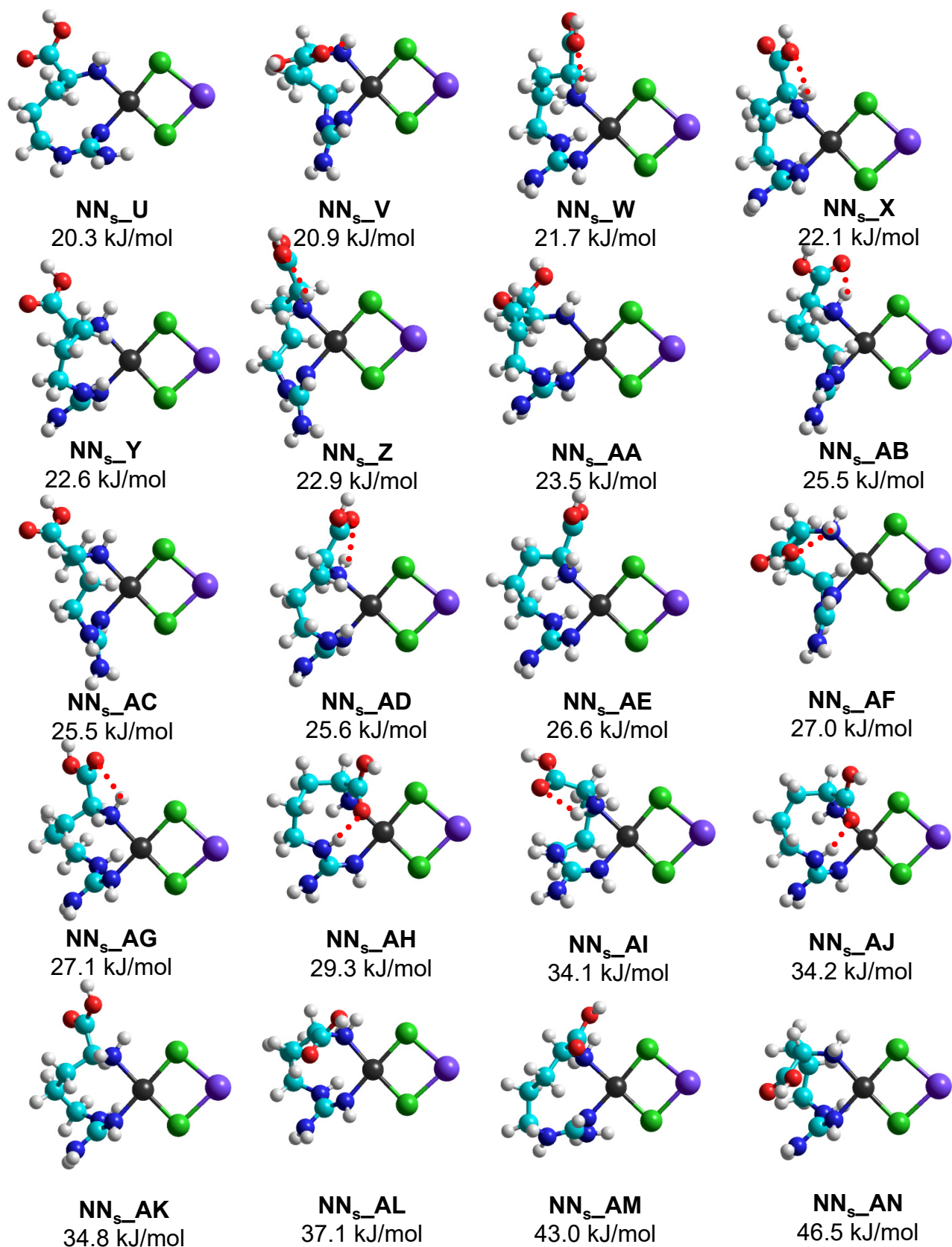
$[(\text{Arg-H})\text{PtCl}_2]^-$, other side chain binding modes

Figure S5.



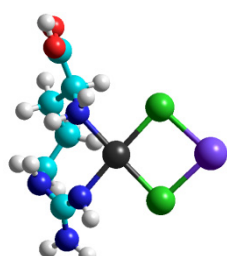
$[(\text{Arg})\text{PtCl}_2+\text{Na}]^+$, NN_s

Figure S5.

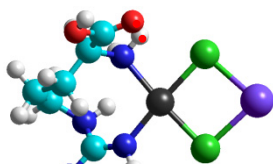


$[(\text{Arg})\text{PtCl}_2+\text{Na}]^+$, NN_s

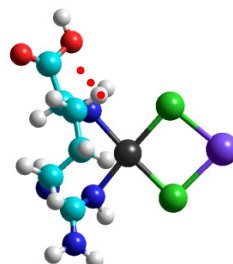
Figure S5.



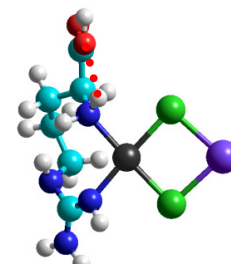
NN_s_AO
50.1 kJ/mol



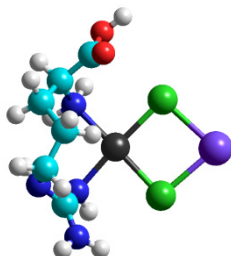
NN_s_AP
53.7 kJ/mol



NN_s_AQ
58.2 kJ/mol



NN_s_AR
67.9 kJ/mol



NN_s_AS
71.9 kJ/mol

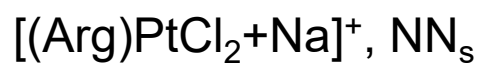


Figure S5.

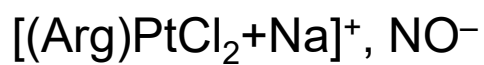
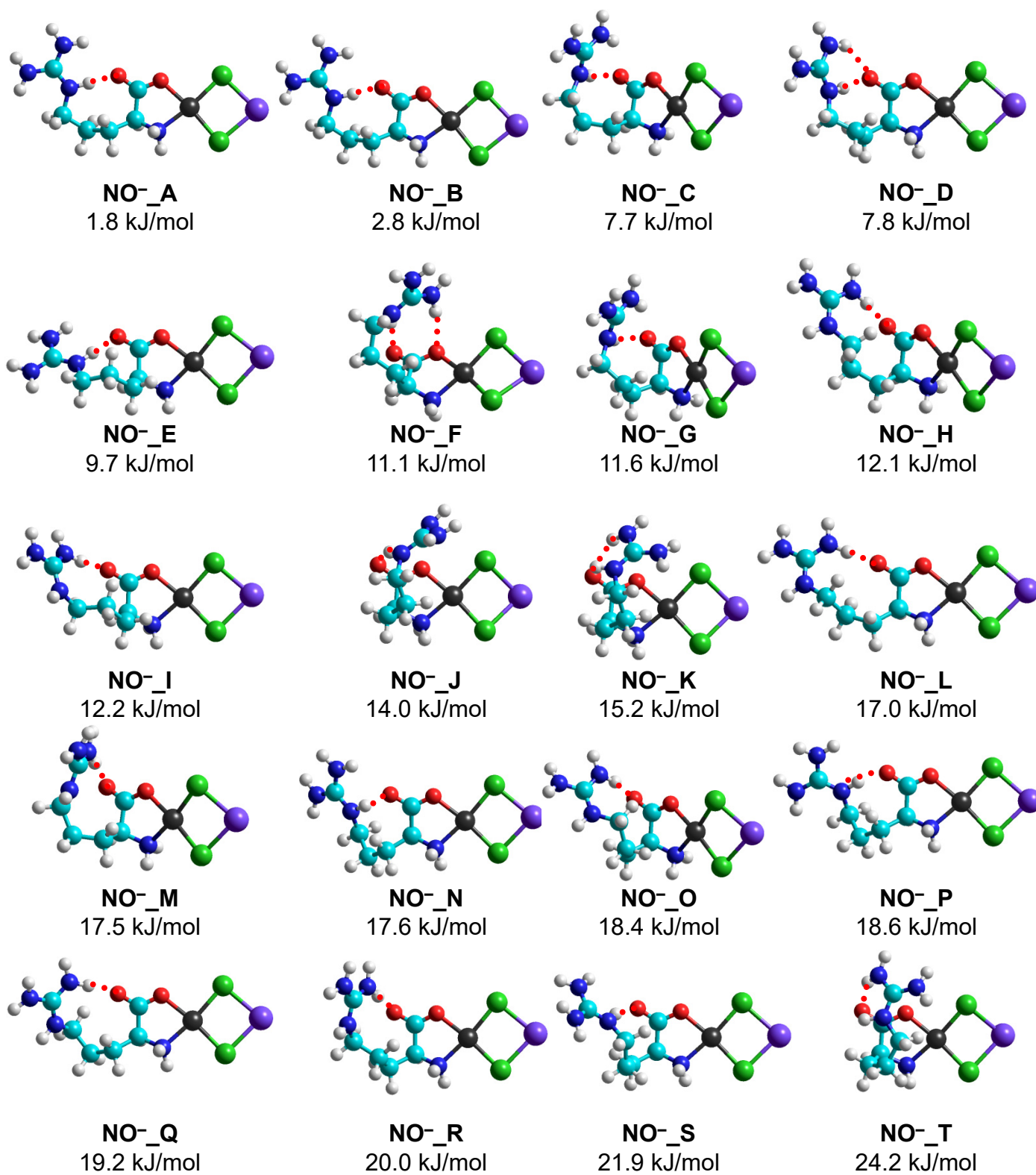


Figure S5.

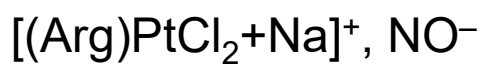
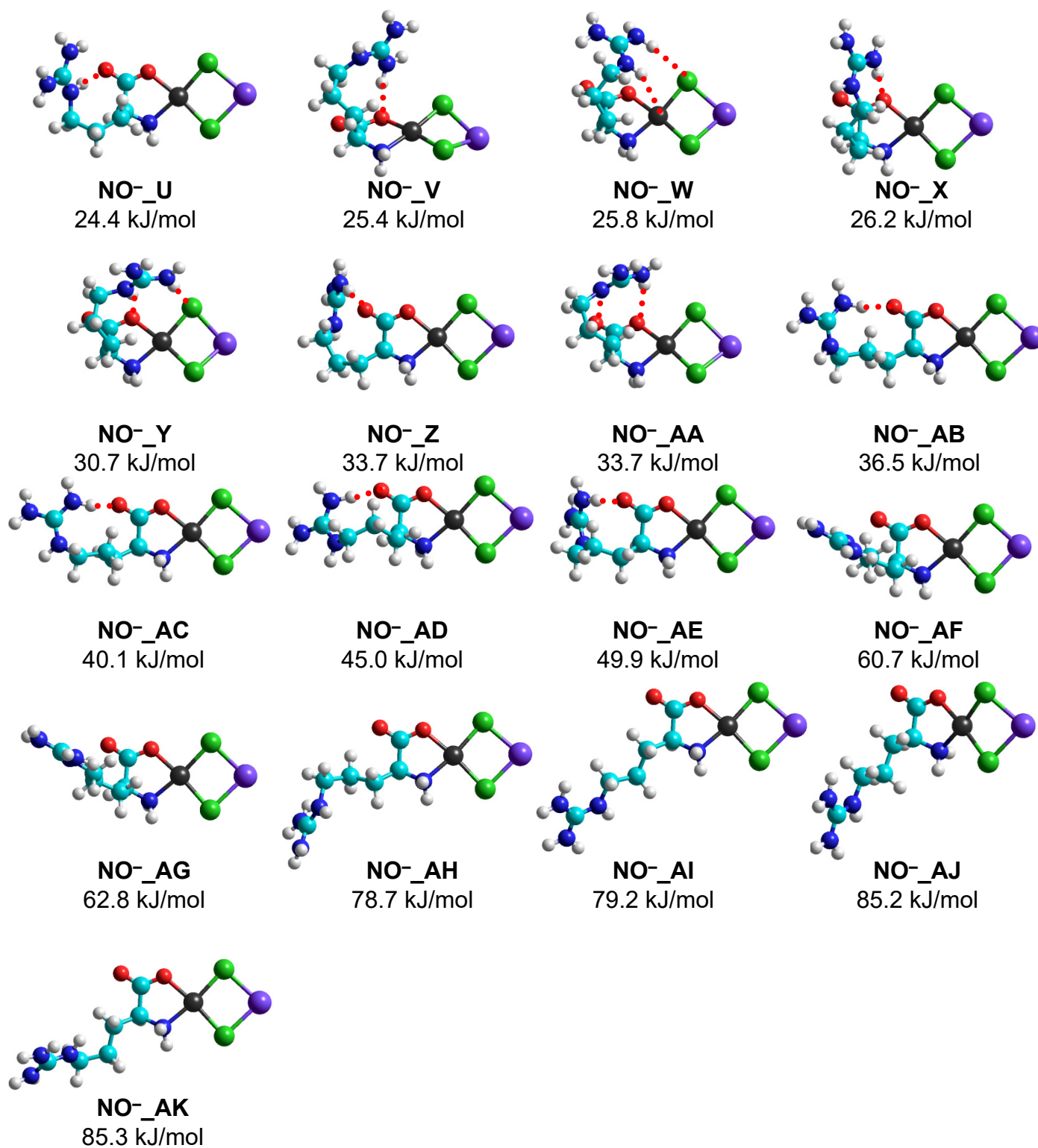
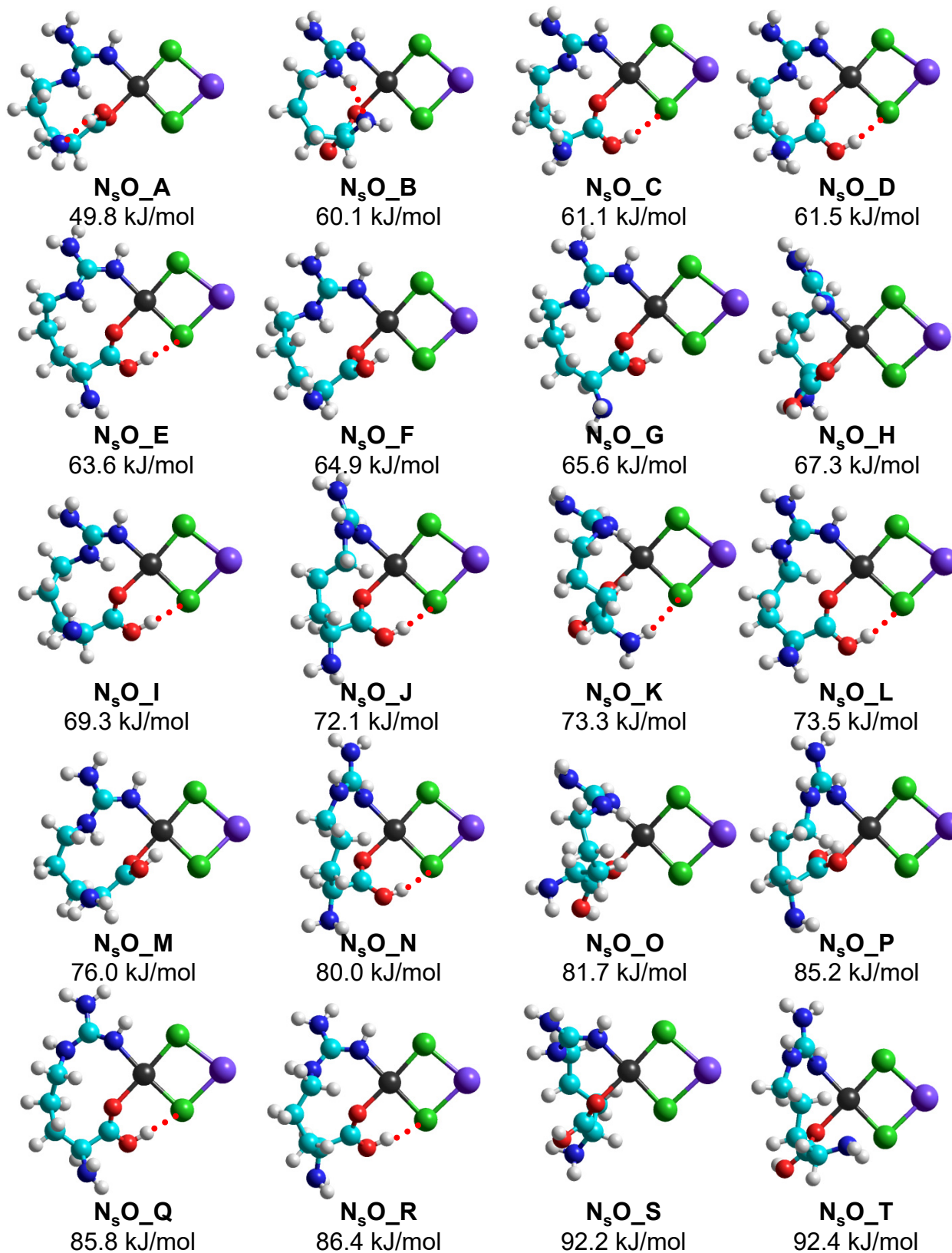


Figure S5.



$[(\text{Arg})\text{PtCl}_2+\text{Na}]^+, \text{N}_s\text{O}$

Figure S5.

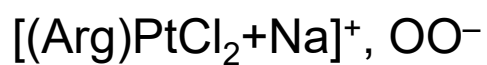
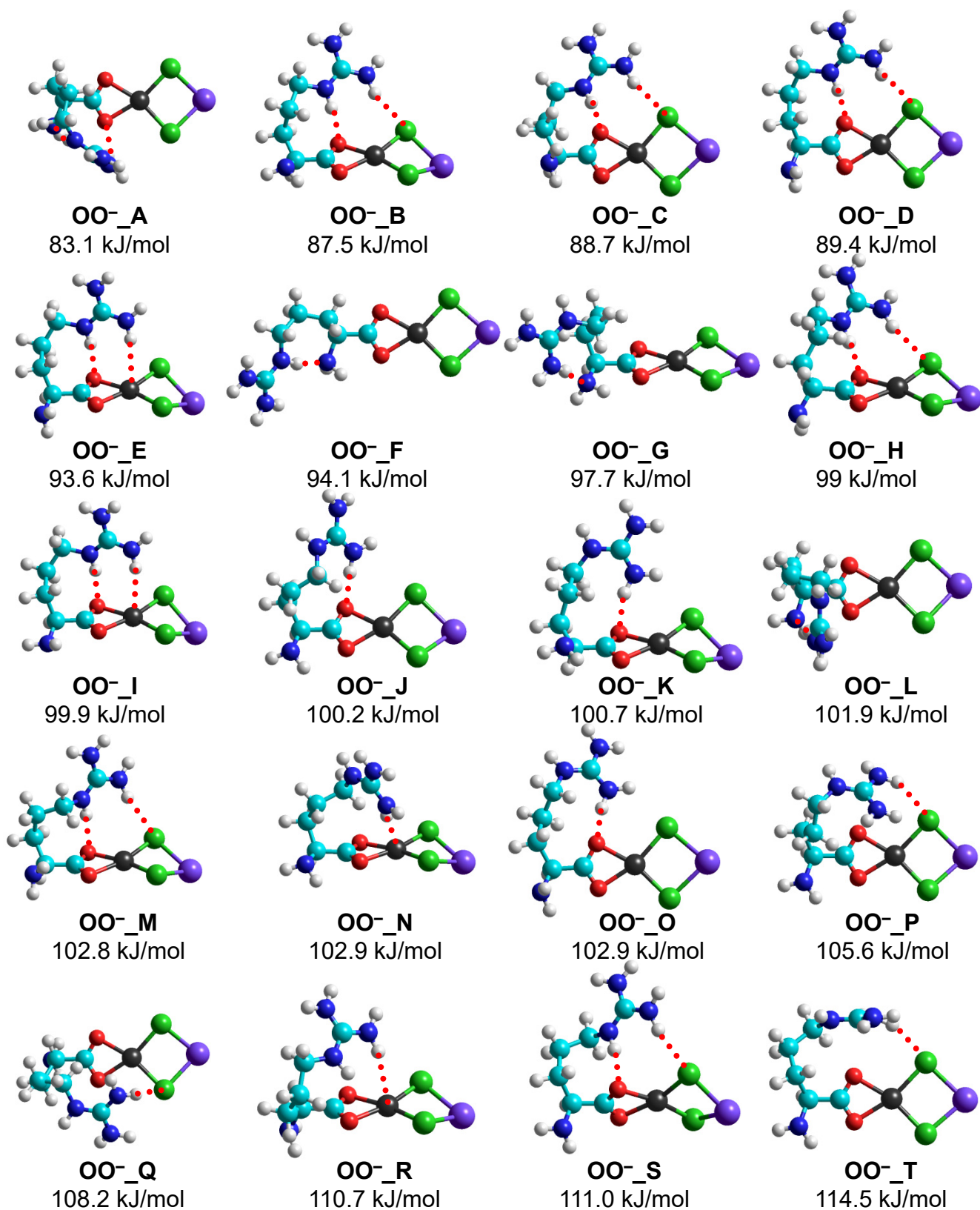
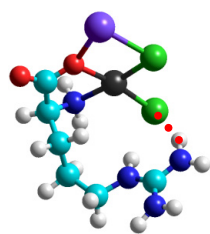


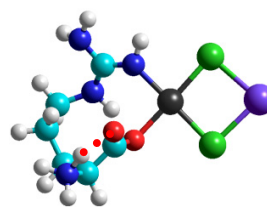
Figure S5.



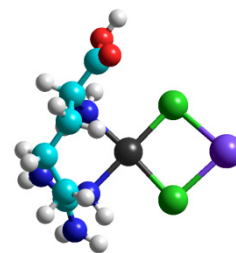
NO⁻_OCl_b_A
21.4 kJ/mol



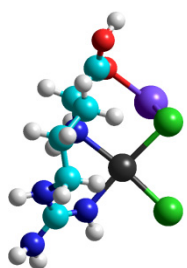
NN_s_OCl_bCl_s_A
36.7 kJ/mol



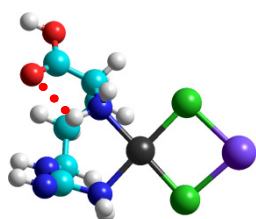
N_sO⁻_A
65.8 kJ/mol



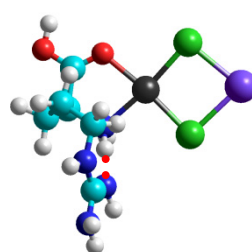
NN_ε_A
67.7 kJ/mol



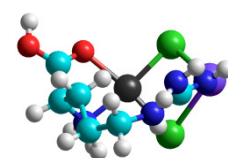
NN_s_OCl_s_A
69.2 kJ/mol



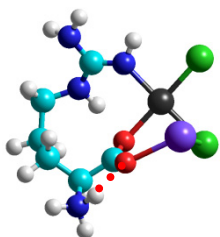
NN_ω_A
80.1 kJ/mol



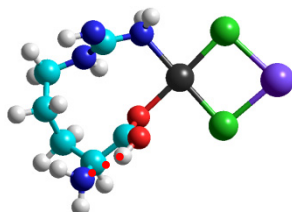
NO_A
84.1 kJ/mol



NO_N_sCl_bCl_o_A
86.5 kJ/mol



N_sO⁻_OCl_s_A
97.7 kJ/mol



N_ωO_A
121.2 kJ/mol



N_εO_A
145.9 kJ/mol

[(Arg)PtCl₂+Na]⁺, Other side chain binding modes

Figure S6.

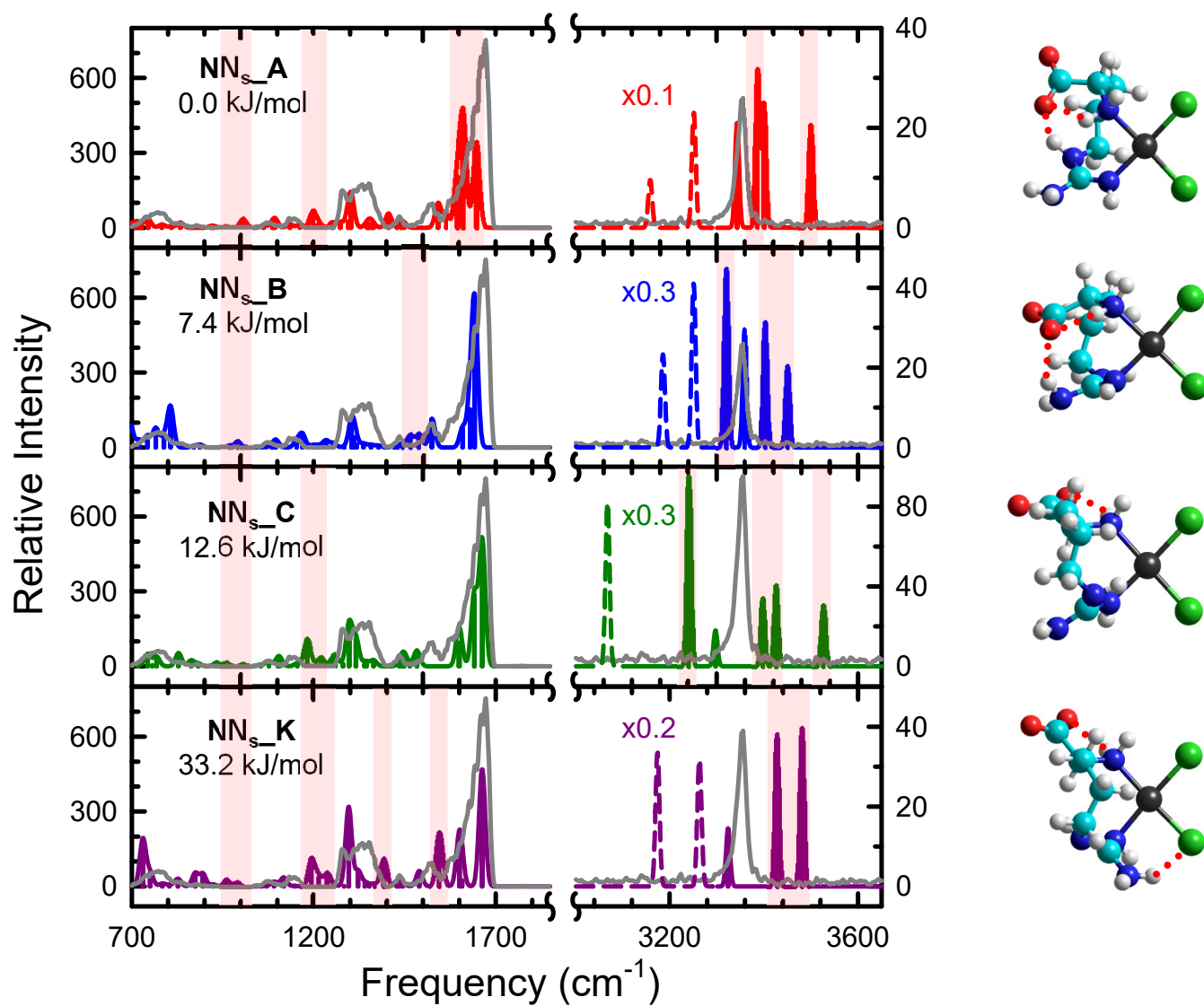


Figure S7.

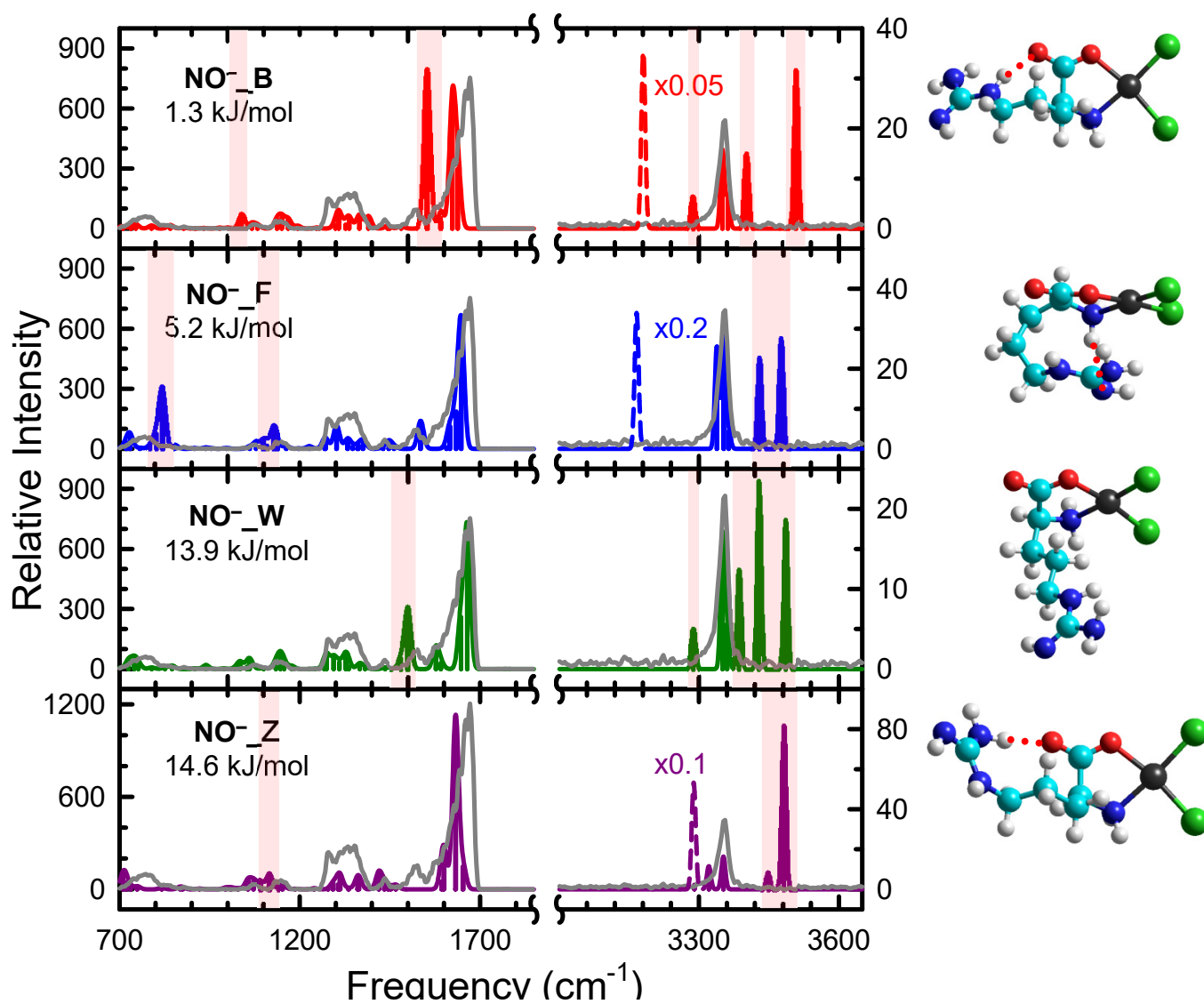


Figure S7.

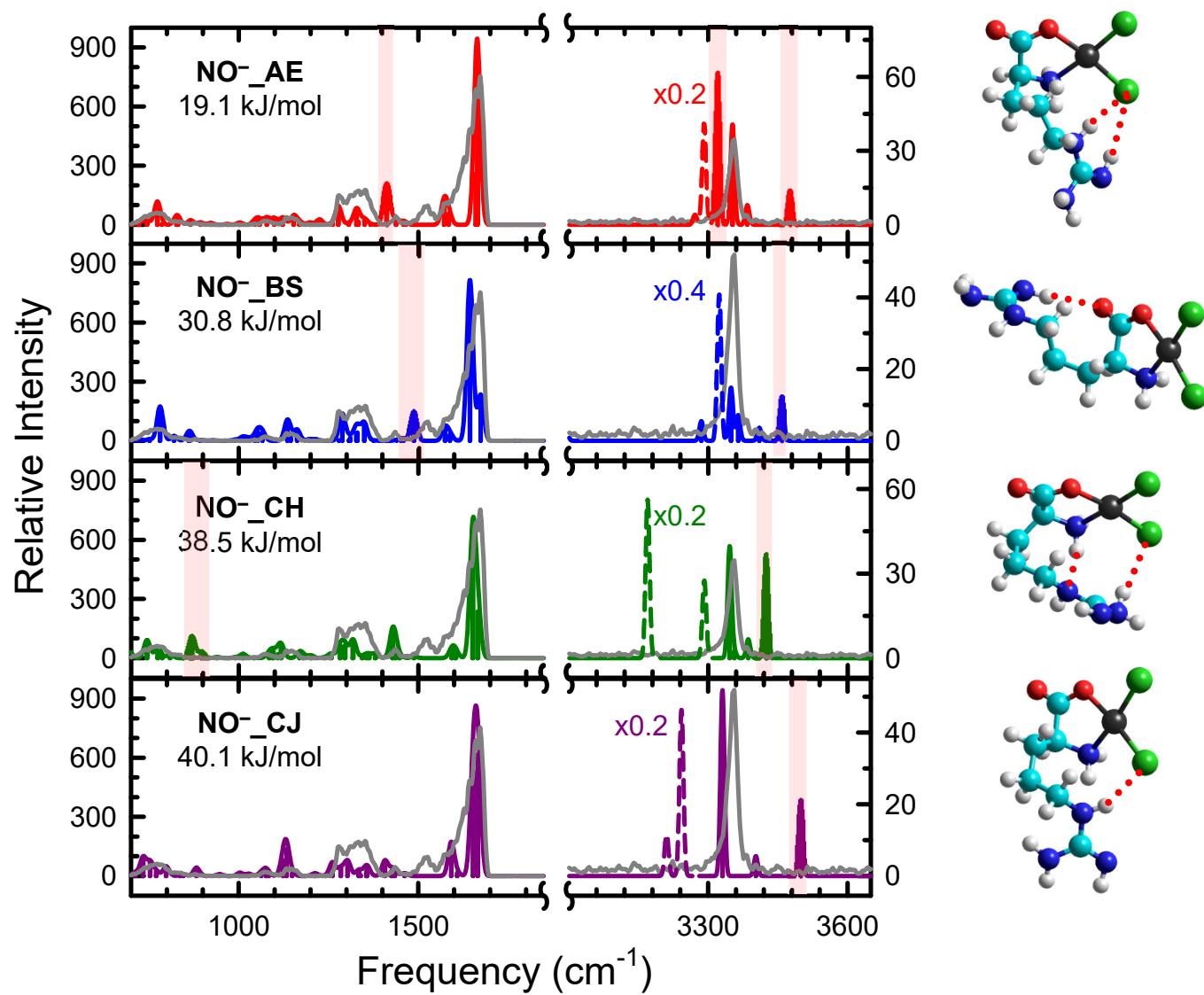


Figure S8.

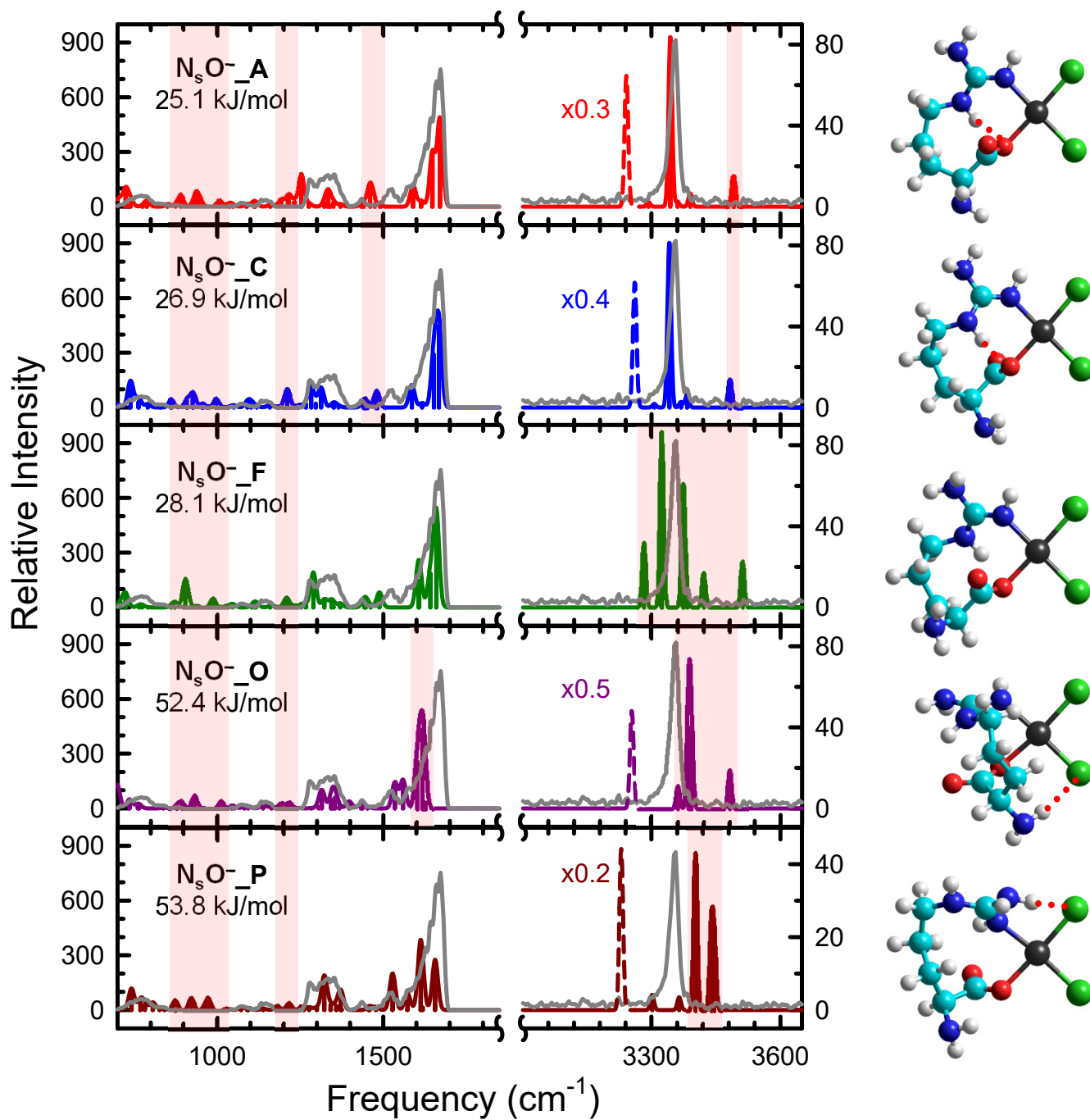


Figure S9.

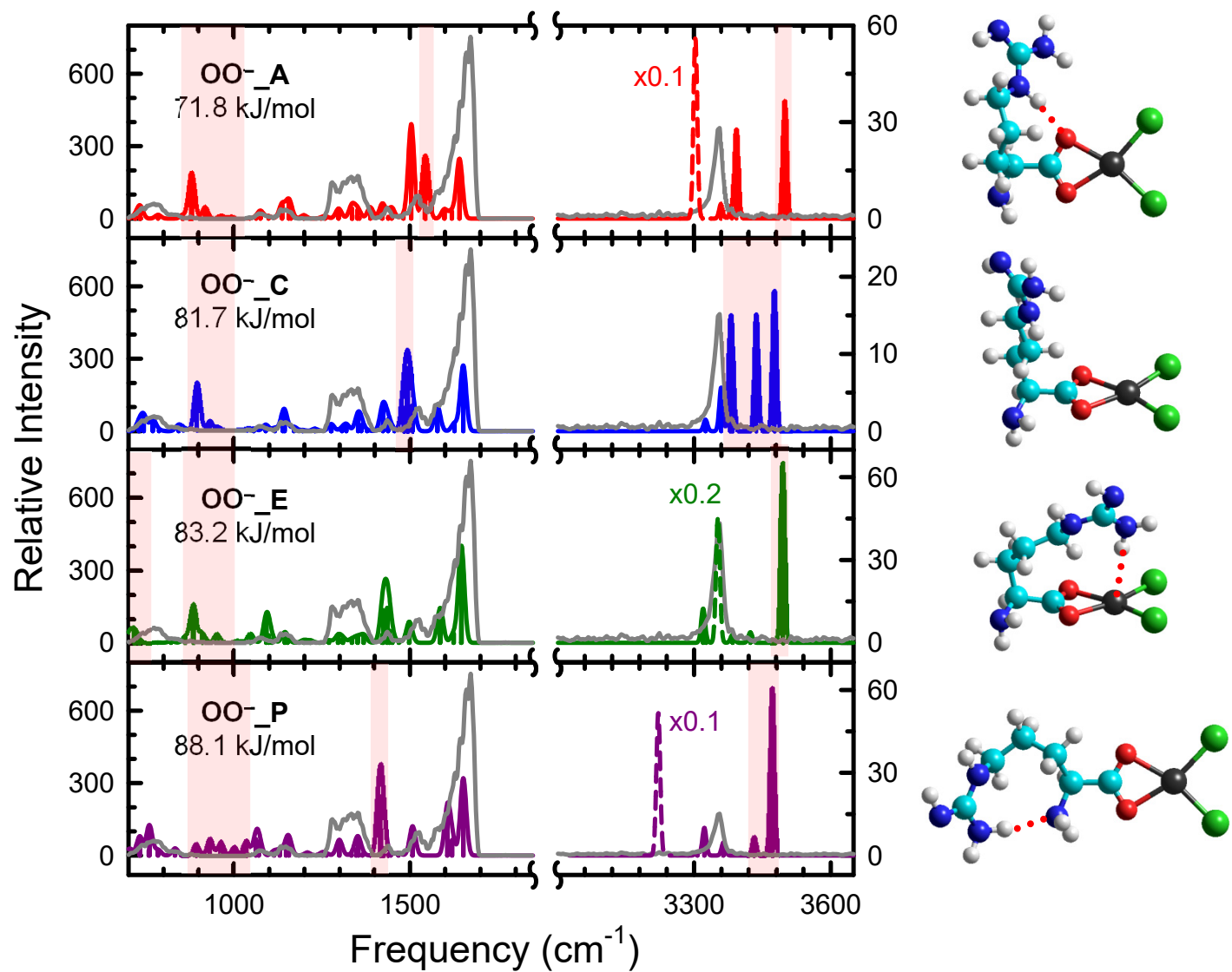
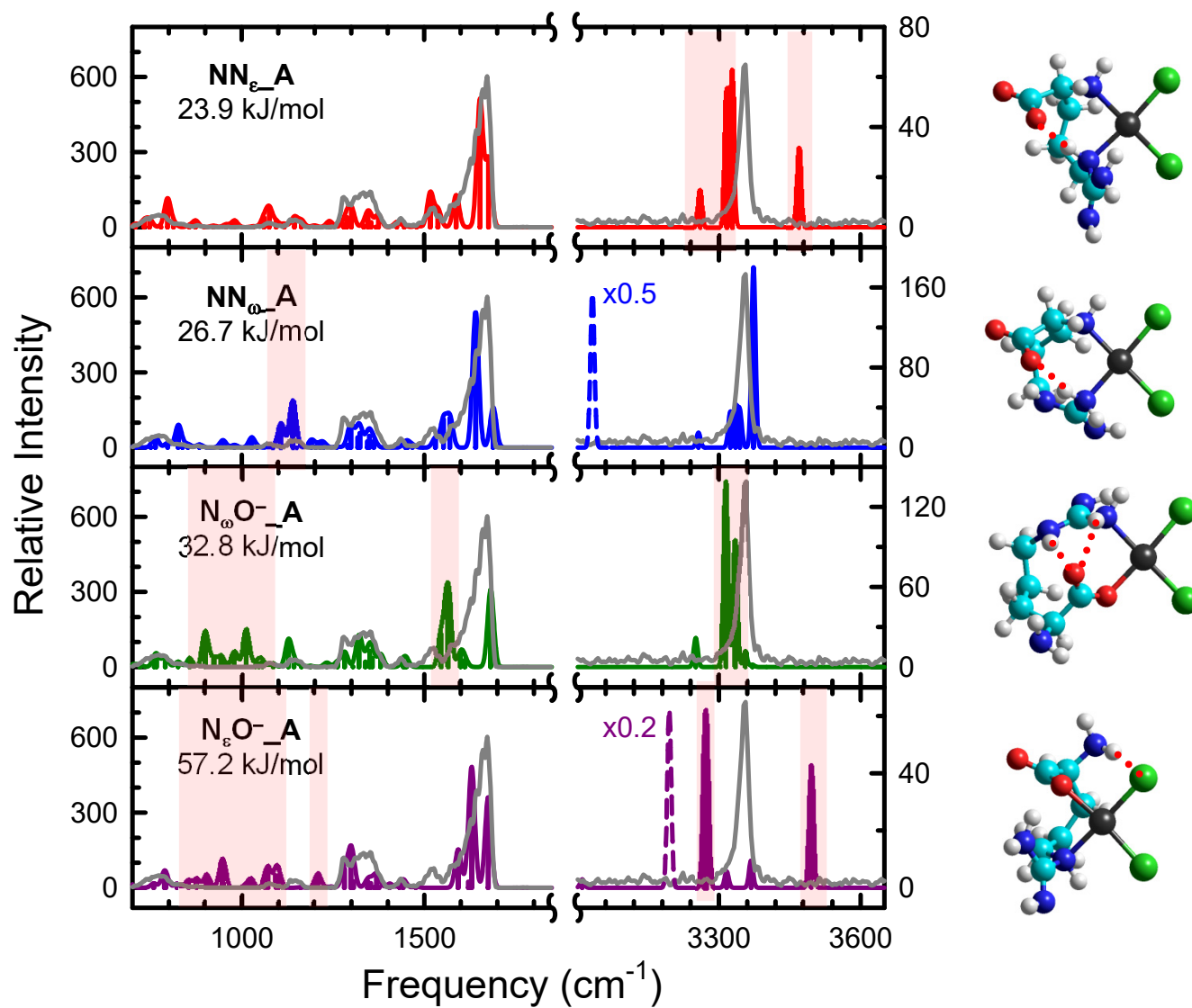


Figure S10.



$[(\text{Arg-H})\text{PtCl}_2]^-$, Other side chain binding modes

Figure S11.

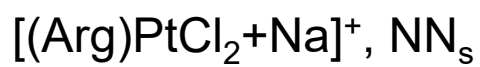
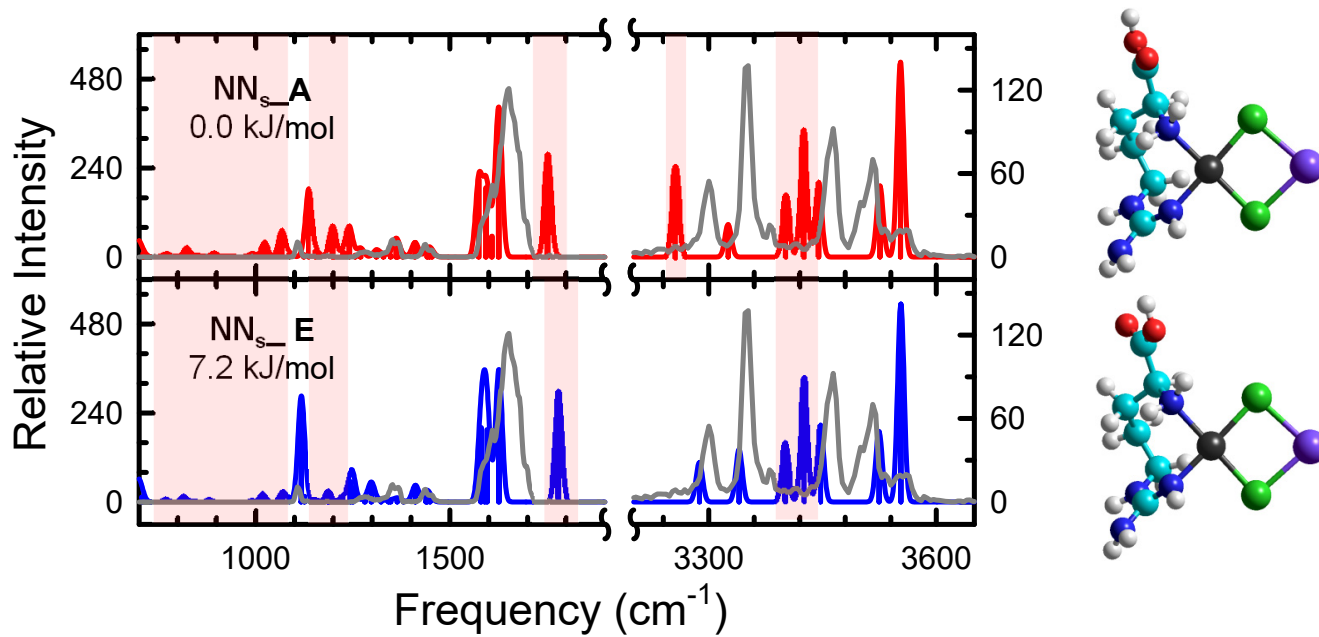


Figure S12.

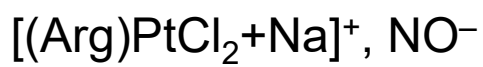
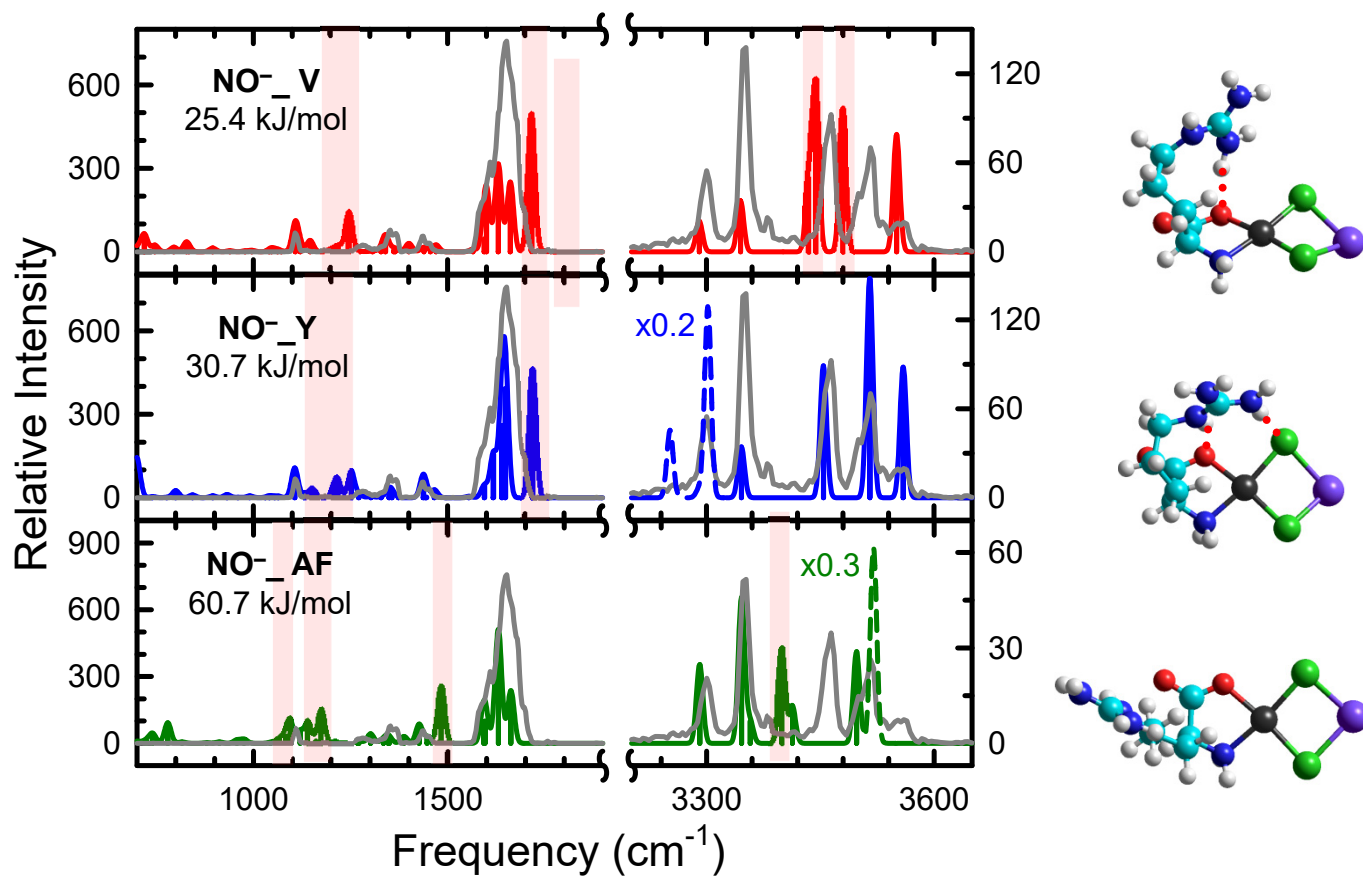


Figure S13.

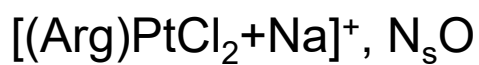
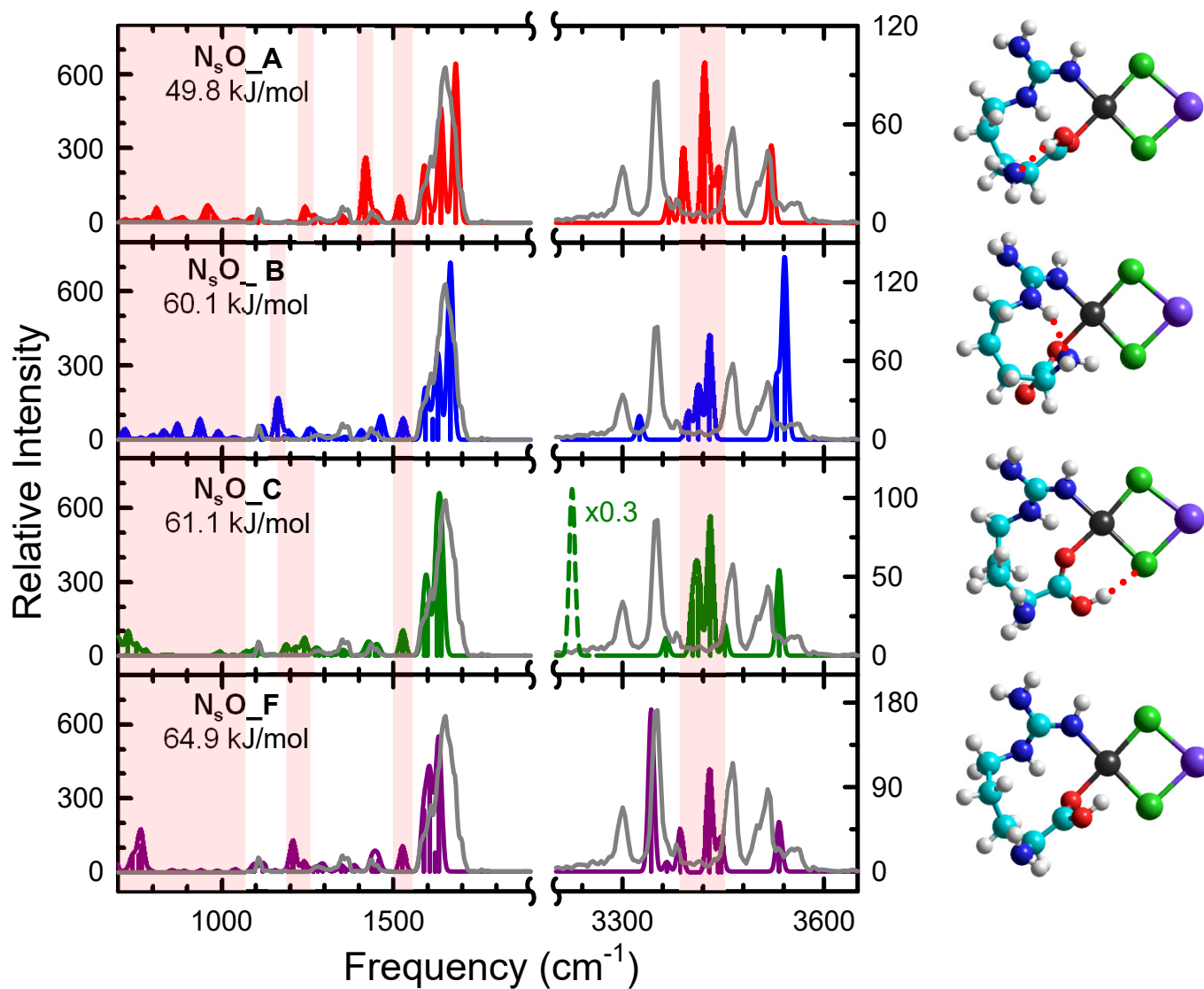


Figure S14.

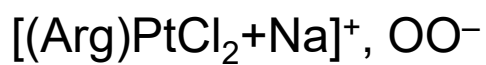
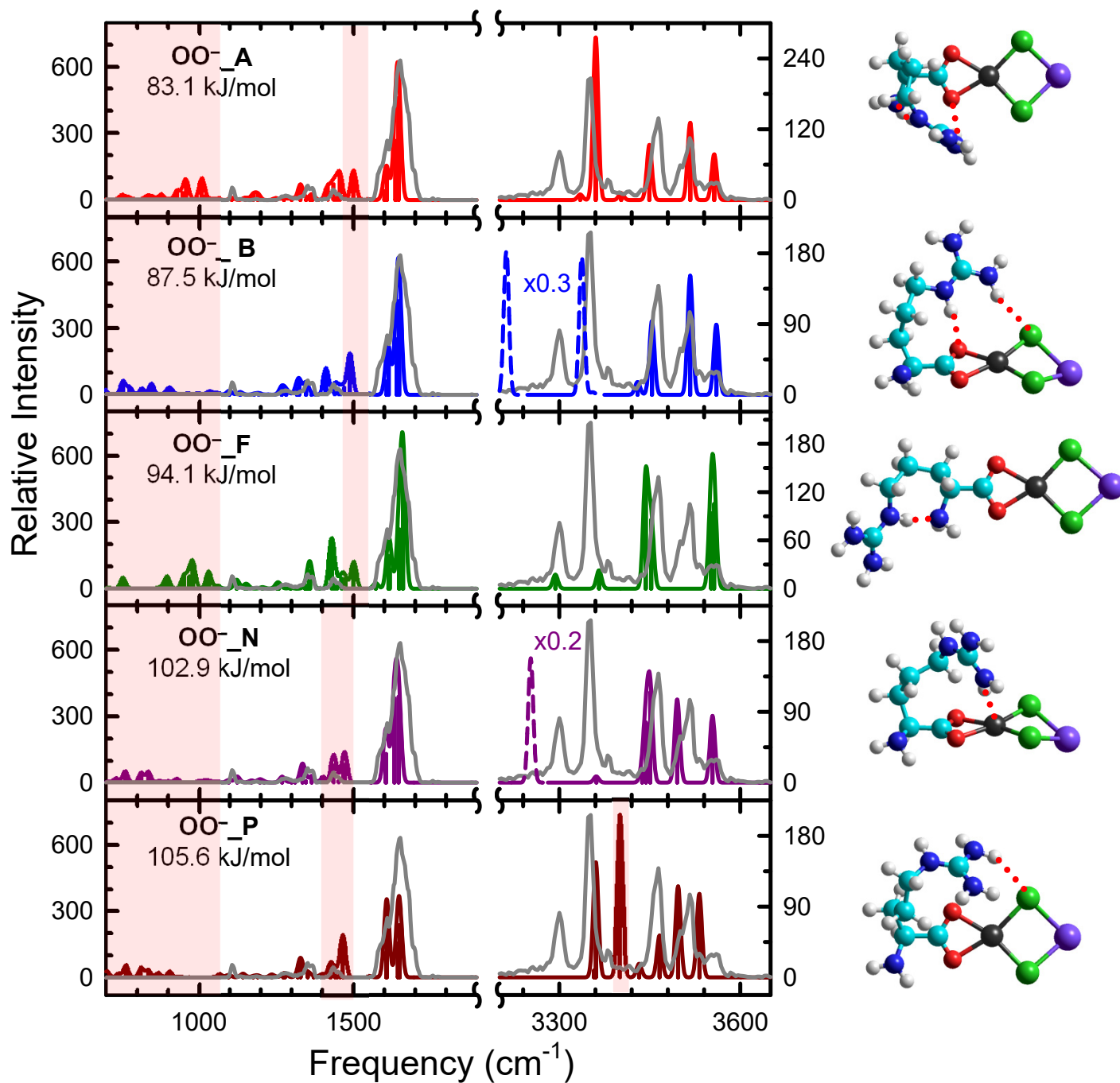
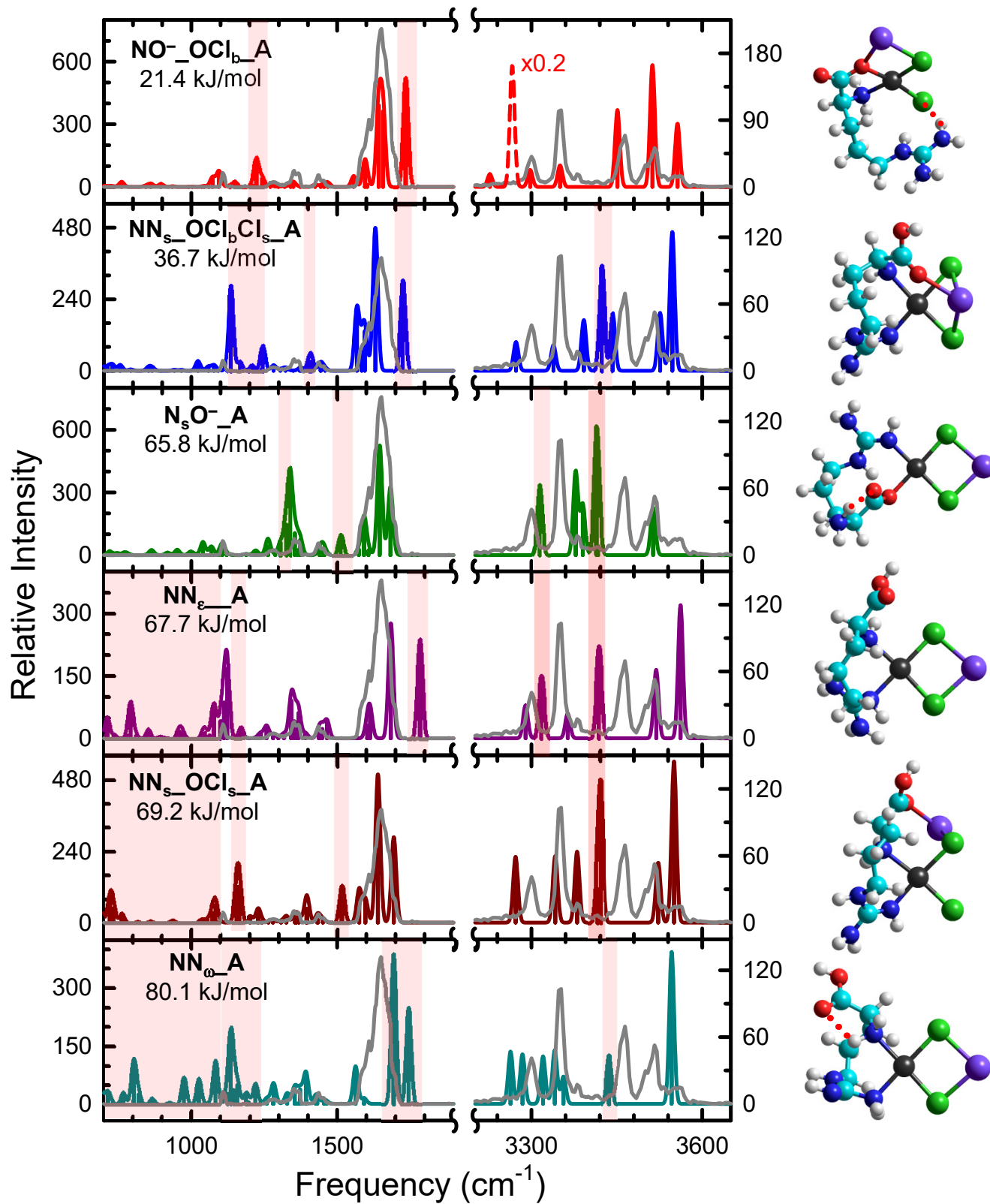
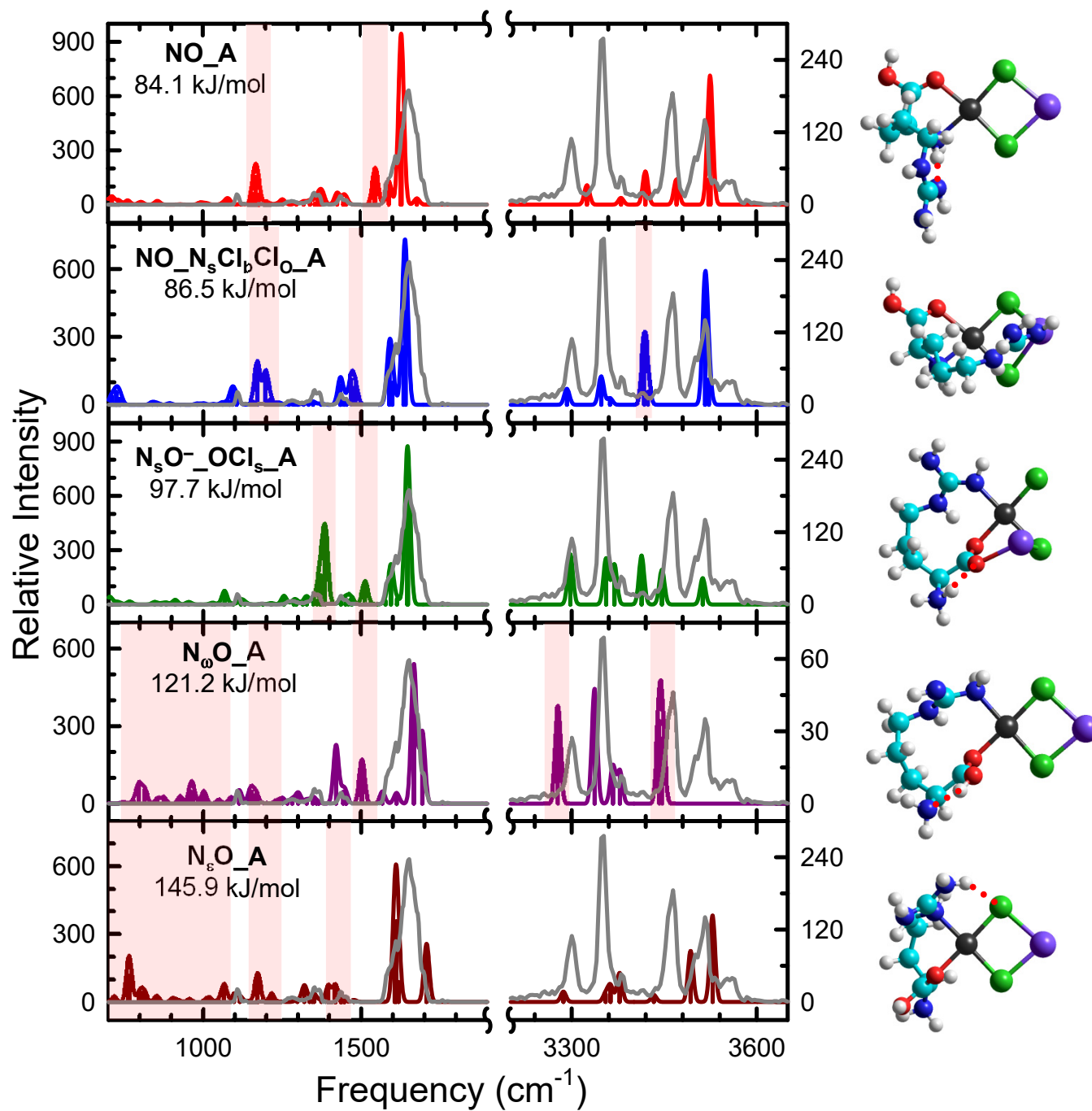


Figure S15.



$[(\text{Arg})\text{PtCl}_2+\text{Na}]^+$, Other side chain binding modes

Figure S15.



$[(\text{Arg})\text{PtCl}_2+\text{Na}]^+$, Other side chain binding modes